Finite Elements in Analysis and Design 206 (2022) 103761

Contents lists available at ScienceDirect

Finite Elements in Analysis & Design

journal homepage: www.elsevier.com/locate/finel

Modeling and simulation of thin-walled piezoelectric energy harvesters immersed in flow using monolithic fluid–structure interaction

Lan Shang [a], Christophe Hoareau [b], Andreas Zilian [a,*]

[a] Department of Engineering, University of Luxembourg, Luxembourg
[b] Laboratoire de Mécanique des Structures et des Systèmes Couplés (LMSSC), Conservatoire national des arts et métiers (Cnam), France

ARTICLE INFO

Keywords:
Fluid–structure interaction
Monolithic coupling
Thin-walled piezoelectric structure
Energy harvester
Pressure discontinuity

ABSTRACT

A monolithic numerical scheme for fluid–structure interaction with special interest in thin-walled piezoelectric energy harvesters driven by fluid is proposed. Employing a beam/shell model for the thin-walled structure in this particular application creates a FSI problem in which an $(n-1)$-dimensional structure is embedded in an n-dimensional fluid flow. This choice induces a strongly discontinuous pressure field along the moving fluid–solid interface. We overcome this challenge within a continuous finite element framework by a splitting-fluid-domain approach. The governing equations of the multiphysics problem are solved in a simultaneous fashion in order to reliably capture the main dynamic characteristics of the strongly-coupled system that involves a large deformation piezoelectric composite structure, an integrated electric circuit and an incompressible viscous fluid. The monolithic solution scheme is based on the weighted residuals method, with the boundary-fitted finite element method used for the discretization in space, and the generalized-α method for discretization in time. The proposed framework is evaluated against reference data of two popular FSI benchmark problems. Two additional numerical examples of flow-driven thin-walled piezoelectric energy harvesters demonstrate the feasibility of the framework to predict controlled cyclic response and limit-cycle oscillations and thus the power output in typical operational states of this class of energy harvesting devices.

1. Introduction

Harvesting energy from ambient flows using piezoelectric structures has become a vibrant research area [1]. This is motivated not only by many practical applications demonstrating that piezoelectric energy harvesters (PEHs) are a promising alternative to conventional batteries for low-power electronic devices, but also by scientific curiosity since flow-driven PEHs are strongly coupled multiphysics systems involving complex interaction between fluid dynamics, structural (electro)mechanics and electric circuits [2,3].

A major challenge in theoretical analyses of flow-driven PEHs consists in predicting the fluid dynamics. Most previous investigations employed potential flow models, e.g., Theodorsen's unsteady thin airfoil theory in [4], the unsteady vortex lattice method in [5,6], the doublet-lattice method in [7], and the state–space model for unsteady aerodynamics in [8]. These models are computationally efficient and one may expect satisfactory results from them when the Reynolds number is reasonably high [9]. However, as pointed out by [10], they fail to precisely capture the viscous effects of the fluid. To obtain a more accurate representation of the driving fluid forces, solving the Navier–Stokes (N-S) equations is an option, although at the cost of greatly increased computational expense. A few papers such as [2,3,10–12] use the N-S equations to model the incompressible viscous flow surrounding PEHs, and paper [13] uses the simplified vorticity description of N-S equations to describe the flow around electromagnetic energy harvesting devices.

In general, numerical study of fluid–structure interaction (FSI) problems based on the N-S equations should first determine the boundary matching method (boundary-fitted or not) and the coupling algorithm (simultaneously solve or not) at the fluid–solid interface. This interface is moving as the immersed structure is deformable and/or non-fixed, so it is straightforward to explicitly track this interface by taking advantage of the classical arbitrary Lagrangian–Eulerian (ALE) description [14], which allows the fluid problem to be solved on a mesh that deforms according to the Lagrangian structure mesh. This boundary-fitted matching approach is easy to implement and accurate, but tends to be tricky when the structural translation/rotation is large or the topology of the fluid domain is changed [15]. In such scenarios, non-boundary-fitted approaches that do not require the fluid mesh to move have been widely used, e.g., the immersed boundary method [16], the fictitious domain method [17] and others. However, considering

* Corresponding author.
E-mail addresses: lan.shang@uni.lu (L. Shang), christophe.hoareau@lecnam.net (C. Hoareau), andreas.zilian@uni.lu (A. Zilian).

https://doi.org/10.1016/j.finel.2022.103761
Received 29 September 2021; Received in revised form 19 January 2022; Accepted 14 March 2022
Available online 8 April 2022
0168-874X/© 2022 The Author(s). Published by Elsevier B.V. This is an open access article under the CC BY-NC-ND license (http://creativecommons.org/licenses/by-nc-nd/4.0/).

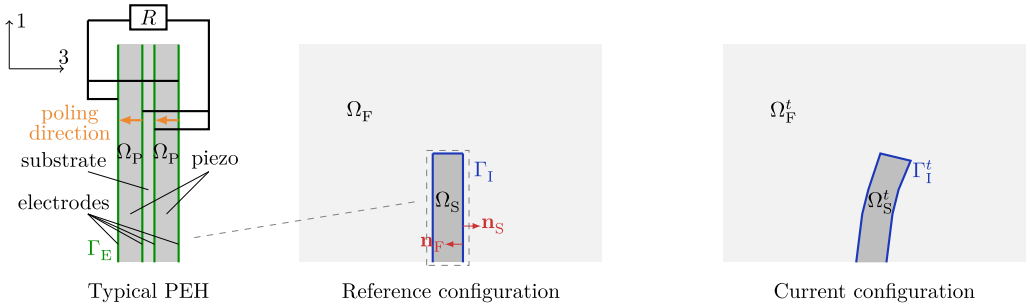


Fig. 1. Reference configuration and current configuration of a typical PEH (in parallel connection) immersed in fluid.

non-boundary-fitted approaches cannot faithfully represent the fluid–solid interface, in the vicinity of which, naturally, the solution accuracy is reduced. More detailed discussion on pros/cons of different boundary matching methods can be found in [18]. As for the coupling algorithm, paper [19] provides a comparative investigation for three available algorithms: partitioned, quasi-direct and monolithic. They distinguish from each other by whether the sub-problems concerned are solved simultaneously or not. The partitioned coupling algorithm seems more popular in FSI community. For instance, the aforementioned papers [2,10–13] all adopt this algorithm, while only [3] is an exception. The reason may be that well-established fluid solvers and solid solvers can be conveniently used for FSI problems in the partitioned algorithm, where the solid and fluid sub-problems are solved separately and then coupled in an iterative fashion. Nevertheless, the monolithic coupling algorithm which solves all field equations at once would be better when perusing improved accuracy and accelerated convergence. In summary, if possible and accuracy is the main focus, normally a boundary-fitted approach combined with a monolithic coupling algorithm should be an advisable scheme to solve the FSI problem of interest. This scheme is the choice of the current work. Actually, exactly the same as [3], in this work, not only the fluid and structure, but also the circuit, are all coupled in a monolithic way.

The fundamental difference between the current work and [3] is that the latter one deals with a three-dimensional structure with small deformation, while the structure in this work may undergo large deformation, and more notably, because one of the most commonly investigated configurations of PEHs is thin-walled beam models [20–22], it would be preferable to employ a geometrically non-volumetric representation for the piezoelectric structure to make best use of these beam models. This representation of a structure causes additional difficulty in FSI problems. As noted by [23], for a velocity–pressure formulation of the N-S equations and no-slip interfacial conditions, embedding a thin structure into a fluid field leads to a strongly discontinuous pressure solution along the moving fluid–solid interface. This difficulty is settled in [23] by a level set method. Paper [23] uses a non-boundary-fitted approach, in which context readers are referred to [15] for deeper discussion on handling the pressure discontinuity. In the context of boundary-fitted approaches, this problem can be addressed by duplicating the interface pressure degrees of freedom [24]. The current paper proposes another simple method to treat pressure discontinuity: splitting the fluid domain by the fluid–solid interface into two parts, which then enables to use two independent pressure variables to represent the discontinuous pressure field.

The remainder of this paper is organized as follows. In Section 2, the governing equations for all fields of interest are introduced, and particularly, the solid is modeled using both volumetric and non-volumetric representations. In Section 3, the monolithic solution scheme based on the weighted residuals method, the approach to tackle strong pressure discontinuity, and the time integration scheme are presented. In Section 4, the models and associated solution scheme are validated against two FSI benchmark examples by numerical experiments. In Section 5, the above framework is extended to study a thin-walled PEH interacting with a flow. Finally, Section 6 summarizes the contributions and specifies the limitations of the current work.

2. Governing equations

Fig. 1 is the schematic illustration of a flow-driven PEH. The PEH comprises an elastic substrate structure, two piezoelectric layers which are covered by electrodes, and a circuit. When the fluid flows, the PEH will deform and convert mechanical energy into electric energy through the piezoelectric effects [25]. Ω_F, Ω_S are the domains occupied by the fluid and the solid in the initial undeformed state (reference configuration), while Ω_F^t, Ω_S^t are the time dependent domains (current configuration). In what follows, we introduce all field equations as well as coupling conditions that govern the behavior of the multiphysics system.

2.1. Fluid

The classical way to describe problems in continuum mechanics is the Lagrangian method for the solid and the Eulerian method for the fluid. In the context of FSI, a common boundary shared by the *computational* domains of the fluid and solid cannot be ensured (note: Γ_I^t is the common *physical* boundary) if using the classical description for the respective standalone problem. Therefore, to develop a closed monolithic model for FSI, one sub-problem, either the fluid or the structure, needs to be formulated in a transformed coordinate system [26]. This system is usually the ALE for the fluid. By ALE, further with the help of mesh motion techniques, the fluid equations can be mapped from one configuration onto another. At this point, there exist two possibilities to formulate a FSI problem in the ALE coordinate: computing the fluid equations in a deformed domain (e.g., [24]) or in a fixed undeformed domain (e.g., [26,27]). Although the fluid equations look much simpler in the former one than those (Eqs. (1)–(2)) in the latter one, we adopt the latter one by transforming all fluid equations onto the reference configuration Ω_F in this work, to facilitate Galerkin-projection based model order reduction as part of future research.

2.1.1. ALE description of the N-S equations on the reference configuration

The flow surrounding a PEH is assumed to be viscous and incompressible, and the fluid dynamics is governed by the N-S equations. In ALE, an auxiliary displacement field $\mathbf{u}_A$ is introduced to realize the transformation of the fluid equations between configurations. The ALE mapping is then defined as $\mathcal{A}(\hat{x},t) = \hat{x} + \mathbf{u}_A(\hat{x},t)$, where $\hat{x}$ is the coordinate of a point in the undeformed domain. The fluid equations formulated on the reference configuration after ALE transformation read [26]

$$\rho_F J_A \frac{\partial \mathbf{v}_F}{\partial t} + \rho_F J_A (\nabla \mathbf{v}_F)\mathbf{F}_A^{-1}(\mathbf{v}_F - \frac{\partial \mathbf{u}_A}{\partial t}) - \nabla \cdot (J_A \mathbf{T}_F \mathbf{F}_A^{-T}) = \mathbf{0} \quad \text{in} \quad \Omega_F, \tag{1}$$

$$\nabla \cdot (J_A \mathbf{F}_A^{-1} \mathbf{v}_F) = 0 \quad \text{in} \quad \Omega_F, \tag{2}$$

where ρ_F, $\mathbf{v}_F$ are the density and velocity of the fluid, respectively; $\mathbf{F}_A := \nabla \mathcal{A} = \mathbf{I} + \nabla \mathbf{u}_A$ is the deformation gradient, and $J_A = \det(\mathbf{F}_A)$ is its determinant; $\mathbf{T}_F$ is the fluid stress tensor, given by the following constitutive law of a Newtonian fluid

$$\mathbf{T}_F + p_F \mathbf{I} - \mu_F((\nabla \mathbf{v}_F)\mathbf{F}_A^{-1} + \mathbf{F}_A^{-T}(\nabla \mathbf{v}_F)^T) = \mathbf{0} \quad \text{in} \quad \Omega_F, \tag{3}$$

with the hydrostatic pressure p_F and the dynamic viscosity μ_F.

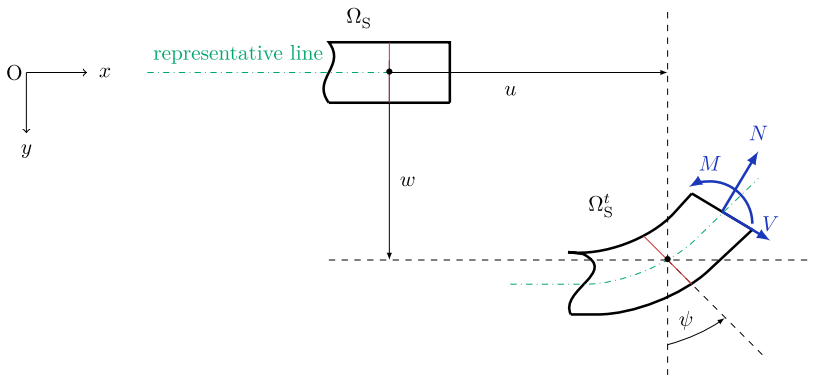


Fig. 2. Planar beam formulation.

2.1.2. Mesh motion model

One basic idea of a monolithic FSI algorithm is to treat the fluid and the solid as a surface-coupled continuum. In this sense, the displacement field $\mathbf{u}_A$ introduced above can be explained as the extension of the structure deformation into the fluid domain, i.e., the fluid mesh motion without any inertial effects. A number of mesh motion models have been proposed, as seen in [28,29], from which, we choose the biharmonic model due to its better mesh performance for large deformation. This model is expressed as

$$\Delta^2 \mathbf{u}_A = \mathbf{0} \quad \text{in} \quad \Omega_F. \tag{4}$$

Furthermore, a mixed formulation with an intermediate variable $\mathbf{z}_A$ and an artificial material parameter ℓ for Eq. (4) can be written as [29]

$$\mathbf{z}_A = -\ell \Delta \mathbf{u}_A, \quad -\ell \Delta \mathbf{z}_A = \mathbf{0} \quad \text{in} \quad \Omega_F. \tag{5}$$

Although the degrees of freedom increase in the finite element implementation because of the new unknown $\mathbf{z}_A$ when comparing Eq. (5) with Eq. (4), we will use Eq. (5) in the later work since it does not require H2-conforming finite elements [29].

2.2. Elastic structure

For the solid field, we take into account two different models: a continuum model and a geometrically nonlinear beam model. The former one coupled with the N-S equations forms a classical FSI setup, thus being appropriate to serve as a reference for a FSI problem when the latter one is used to model the structure. The electromechanical model of the thin-walled PEH driven by a flow under consideration is also built based on the latter one.

2.2.1. Continuum solid model

The linear momentum balance equation of a solid undergoing large deformation in the Lagrangian Coordinate System with respect to (w.r.t.) the fixed reference configuration Ω_S is

$$\rho_S \frac{\partial^2 \mathbf{u}_S}{\partial t^2} - \nabla \cdot (\mathbf{F}_S \mathbf{S}_S) = \mathbf{0} \quad \text{in} \quad \Omega_S, \tag{6}$$

where ρ_S is the solid density, $\mathbf{u}_S$ is the solid displacement, $\mathbf{F}_S = \mathbf{I} + \nabla \mathbf{u}_S$ is the deformation gradient, and $\mathbf{S}_S$ is the second Piola–Kirchhoff stress tensor given by

$$\mathbf{S}_S - \lambda_S (\mathrm{tr}\mathbf{E}_S)\mathbf{I} - 2\mu_S \mathbf{E}_S = \mathbf{0} \quad \text{in} \quad \Omega_S \tag{7}$$

using the St. Venant-Kirchhoff material law with the Green–Lagrange strain tensor $\mathbf{E}_S = \frac{1}{2}(\mathbf{F}_S^T \mathbf{F}_S - \mathbf{I})$. λ_S, μ_S are the Lamé coefficients. In the FSI coupling, the structural velocity $\mathbf{v}_S$ but not the displacement $\mathbf{u}_S$ is used as the primary variable. The relation between them is

$$\mathbf{v}_S - \frac{\partial \mathbf{u}_S}{\partial t} = \mathbf{0} \quad \text{in} \quad \Omega_S. \tag{8}$$

It is pertinent to mention here that another method is available in literature to express the governing equations of the solid, i.e., the first-order time rate (of velocity) formulation for both Eq. (6) and Eq. (7), as seen in [3,23,30]. The benefit of the rate formulation is that when coupled with a flow (Eqs. (1)–(3)), a system composed of equations concerning only first-order differential w.r.t. time is achieved. This property can help to avoid the problems with the time integration scheme encountered in Section 3.4, but at the meantime, an additional primary unknown, i.e., the stress for the solid, needs to be solved. What is more, if large deformation is of interest, the solid displacement will remain in the stress expression, and thus computing the displacement by integrating the velocity over time is still inevitable [23,30]. Therefore, we adopt the more common formulation of the governing equations Eqs. (6)–(7) for the solid in this work.

2.2.2. Geometrically nonlinear beam model

The electromechanical model of the flow-driven PEH under consideration is based on a beam model that allows for large deformation in the $O-xy$ plane, as seen in Fig. 2.

A general expression for the equilibrium of a beam subject to plane deformation in the Lagrangian Coordinate System may be formulated for the deformed segment (current state) w.r.t. the reference configuration as

$$\rho_S \mathbf{G}_S \frac{\partial^2 \mathbf{d}_S}{\partial t^2} - \mathfrak{R}(\mathbf{s}_S) - \mathbf{f}_F = \mathbf{0} \quad \text{in} \quad \Omega_S. \tag{9}$$

In Eq. (9), Ω_S is geometrically a line to represent the physical beam, and naturally we have $\Omega_S = \Gamma_I$; $\mathbf{d}_S = [u, w, \psi]^T$ is a vector collecting the axial (in the beam length direction, i.e., x-direction in Fig. 2) displacement u, transverse (in the beam thickness direction, y-direction) displacement w and cross-section rotation ψ of the beam, and in this case, we denote $[u, w]^T$ by $\mathbf{u}_S$, $[\frac{\partial u}{\partial t}, \frac{\partial w}{\partial t}, \frac{\partial \psi}{\partial t}]^T = [u_t, w_t, \psi_t]^T$ by $\mathbf{d}_{S,t}$, and $[u_t, w_t]^T$ by $\mathbf{v}_S$; $\mathbf{f}_F$ is the external fluid force acting on the beam pulled back to the reference configuration in a FSI context, including two components (force in x- and y-direction, but no bending moment); $\mathbf{G}_S$ is a diagonal matrix to describe the cross-section geometry, given by

$$\mathbf{G}_S = \begin{bmatrix} b_S h_S & 0 & 0 \\ 0 & b_S h_S & 0 \\ 0 & 0 & b_S h_S^3/12 \end{bmatrix}, \tag{10}$$

where b_S is the beam width and h_S is the beam thickness; $\mathfrak{R}(\mathbf{s}_S)$ indicates the elastic behavior of the beam with the internal force vector $\mathbf{s}_S = [N, V, M]^T$, where the components are the normal force, shear force and bending moment, respectively, given by

$$\mathbf{s}_S = \mathbf{K}_S \mathbf{G}_S \mathbf{C}_S \mathbf{e}_S, \tag{11}$$

with

$$\mathbf{K}_S = \begin{bmatrix} 1+\varepsilon & 0 & \kappa \\ \tau & 1 & 0 \\ 0 & 0 & 1+\varepsilon \end{bmatrix}, \quad \mathbf{C}_S = \begin{bmatrix} c_S & 0 & 0 \\ 0 & \frac{c_S}{2(1+\nu_S)} & 0 \\ 0 & 0 & c_S \end{bmatrix}, \quad \mathbf{e}_S = [\varepsilon, \tau, \kappa]^T. \tag{12}$$

In Eq. (12), $\mathbf{C}_S$ is the material parameter matrix, where c_S is the Young's modulus and ν_S is the Poisson ratio; $\mathbf{e}_S$ is a vector collecting the beam strain measures, i.e., the axial strain ε, shear strain τ and curvature κ; $\mathbf{K}_S$ is used to transform the stress resultants obtained directly by the constitutive law from the reference configuration to the current configuration. Considering the strains are small, it is safe to take $\mathbf{K}_S = \mathbf{I}$. This work adopts geometrically exact kinematics [31] with the assumption of the rigid beam cross-section, based on which $\mathbf{e}_S$ is expressed as

$$\mathbf{e}_S = [(1+u')\cos\psi - w'\sin\psi - 1, \quad (1+u')\sin\psi + w'\cos\psi, \quad \psi']^{\mathrm{T}}, \tag{13}$$

where $(\cdot)'$ refers to the differential w.r.t. the local axial coordinate x associated with the reference configuration.

For brevity, the elastic term $\mathfrak{R}(\mathbf{s}_S)$ is not explicitly expressed in this work, but it can be easily found in literature such as [31]. In addition, a displacement-based weak form of the beam model deriving from the virtual work formulated w.r.t. the reference configuration is given in [32], which also presents a continuum-mechanics interpretation of the geometrically exact beam model used here. One could refer to [23] to seek the balance equation of a thin-walled structure formulated in a form more similar to Eq. (6), i.e., the deformation gradient being included. This form is not applied here because we would like to keep consistent with the expression most commonly used for a beam model, and apparently, it is also easier to compare Eq. (9) rather than the formulation used in [23] with the authors' previous work [33] that focuses on building an electromechanical model for beam-like PEHs.

2.3. Piezoelectric layers

The model of the piezoelectric layers is almost the same as that of the elastic structure shown in Section 2.2.2, with the main difference in the constitutive relations. For piezoelectric materials, piezoelectric effects need to be included. Letting $\mathbf{s}_P = [N, V, M, D_3]^{\mathrm{T}}$, $\mathbf{e}_P = [\varepsilon, \tau, \kappa, E_3]^{\mathrm{T}}$, where D_3 is the electric displacement and E_3 is the electric field, with the subscript 3 indicating the variable is in the 3−direction (shown in Fig. 1), the constitutive relation is

$$\mathbf{s}_P = \mathbf{G}_P\mathbf{C}_P\mathbf{e}_P, \tag{14}$$

with

$$\mathbf{G}_P = \begin{bmatrix} b_P h_P & 0 & 0 & 0 \\ 0 & b_P h_P & 0 & 0 \\ 0 & 0 & b_P h_P^3/12 & 0 \\ 0 & 0 & 0 & 1 \end{bmatrix}, \quad \mathbf{C}_P = \begin{bmatrix} c_P & 0 & 0 & -e_{31} \\ 0 & \frac{c_P}{2(1+\nu_P)} & 0 & 0 \\ 0 & 0 & c_P & 0 \\ e_{31} & 0 & 0 & \epsilon_{33}^S \end{bmatrix}, \tag{15}$$

where the subscript $(\cdot)_P$ means the parameter is for the piezoelectric material, and the new parameters e_{31}, ϵ_{33}^S are the piezoelectric constant and permittivity, respectively.

Two other equations, i.e., the kinematics for the new variable E_3 and the equilibrium for D_3, should also be given to close the governing equations of the piezoelectric layers:

$$E_3 = \mathfrak{F}(\phi) \quad \text{in} \quad \Omega_P, \tag{16}$$

$$\frac{\partial D_3}{\partial y} = 0 \quad \text{in} \quad \Omega_P, \tag{17}$$

where $\mathfrak{F}(\phi)$ indicates the relation between E_3 and the voltage output ϕ, dependent on the PEH configuration [20], and Eq. (17) is the differential form of Gauss' law applied to a PEH where the electrodes are perpendicular to 3-direction [20].

2.4. Electrodes and circuit

The electrodes with a negligible thickness (Γ_E in Fig. 1) covering the surfaces of the piezoelectric layers collect free electric charges during deformation and help to make a usable circuit. The net charge Q passing through the electrodes also depends on the PEH configuration and can be given by Gauss' law [20]. According to Ohm's law, the electric current in a circuit bearing a resistive load R is $I_c = \frac{\phi}{R}$, while from the definition of the electric current, we have $I_c = \frac{\mathrm{d}Q}{\mathrm{d}t}$. These two expressions are used to form the electrode–circuit coupling condition:

$$\frac{\mathrm{d}Q}{\mathrm{d}t} - \frac{\phi}{R} = 0 \quad \text{on} \quad \Gamma_E. \tag{18}$$

2.5. Coupling conditions

For a flow-driven PEH, besides the coupling between the fluid and structure, which can be seen as the exterior coupling, the PEH itself is also a multiphysics system including the interior piezo-elastodynamics coupling and electrode–circuit coupling (Eq. (18)). The focus of this paper is on the exterior coupling, as the interior coupling of thin-walled PEHs has been investigated in the authors' previous work [33]. Therefore, only FSI coupling conditions are presented below.

At the fluid–solid interface Γ_I on the reference configuration, the following geometrical, kinematic and dynamic conditions should be fulfilled:

$$\mathbf{u}_A - \mathbf{u}_S = \mathbf{0} \quad \text{on} \quad \Gamma_I, \tag{19}$$

$$\mathbf{v}_F - \mathbf{v}_S = \mathbf{0} \quad \text{on} \quad \Gamma_I, \tag{20}$$

$$J_A\mathbf{T}_F\mathbf{F}_A^{-\mathrm{T}}\mathbf{n}_F + \mathbf{F}_S\mathbf{S}_S\mathbf{n}_S = \mathbf{0} \quad \text{on} \quad \Gamma_I. \tag{21}$$

In Eq. (21), $\mathbf{n}_F, \mathbf{n}_S$ are unit outward normal vectors opposite to each other (see in Fig. 1). Eqs. (19)–(20) also hold for the beam model in Section 2.2.2, but the dynamic coupling condition Eq. (21) becomes [24]

$$[\![J_A\mathbf{T}_F\mathbf{F}_A^{-\mathrm{T}}\mathbf{n}_F]\!] + \mathbf{f}_F = 0 \quad \text{on} \quad \Gamma_I, \tag{22}$$

where Γ_I is the representative line of the beam itself, $[\![\cdot]\!]$ means the jump of the fluid dynamic stress through the immersed (non-volumetric) thin-structure resulting from the pressure and velocity which are respectively strongly and weakly (gradient) discontinuous along the fluid–solid interface [23,24]. It should also be noted that the beam cross-section rotation ψ has no coupling relation with the fluid field.

2.6. Boundary conditions and initial conditions

In mathematics, the above governing equations make up a partial differential equation (PDE) system w.r.t. the position and time. To obtain a specific solution to the PDE system, boundary conditions (BCs) and initial conditions (ICs) are required. The general expressions of BCs and ICs are available from many papers such as [3,24,30], so we do not repeat them here, whereas BCs and ICs for particular problems in Sections 4 and 5 will be clearly presented at corresponding parts.

3. Monolithic solution scheme

We consider a monolithic solution scheme deriving from the weighted residuals method on the reference configuration to three subproblems: (I) a volumetric continuum solid, (II) a non-volumetric elastic beam and (III) a non-volumetric PEH, all coupled with a flow. A unified framework applies to the three, but for the latter two, more unknown variables are concerned, and the strong discontinuity of the pressure solution should be properly tackled.

3.1. Weak forms

The numerical method to solve the PDE system of interest in this work is the finite element method, so weak forms are presented in the succeeding text.

3.1.1. Fluid

Assuming Dirichlet conditions on the fluid boundary excluding the fluid–solid interface (i.e., $\partial\Omega_{\mathrm{F}}\backslash\Gamma_{\mathrm{I}}$) for simplicity, the weak form of the N-S Eqs. (1)–(2) with test functions $\delta\mathbf{v}_{\mathrm{F}}$, δp_{F} is

$$\int_{\Omega_{\mathrm{F}}}(\rho_{\mathrm{F}}J_{\mathrm{A}}(\frac{\partial\mathbf{v}_{\mathrm{F}}}{\partial t}+(\nabla\mathbf{v}_{\mathrm{F}})\mathbf{F}_{\mathrm{A}}^{-1}(\mathbf{v}_{\mathrm{F}}-\mathbf{v}_{\mathrm{A}}))\cdot\delta\mathbf{v}_{\mathrm{F}}+J_{\mathrm{A}}\mathbf{T}_{\mathrm{F}}\mathbf{F}_{\mathrm{A}}^{-\mathrm{T}}:(\nabla\delta\mathbf{v}_{\mathrm{F}}))\mathrm{d}x$$
$$-\int_{\Gamma_{\mathrm{I}}}J_{\mathrm{A}}\mathbf{T}_{\mathrm{F}}\mathbf{F}_{\mathrm{A}}^{-\mathrm{T}}\mathbf{n}_{\mathrm{F}}\cdot\delta\mathbf{v}_{\mathrm{F}}\mathrm{d}s=0\quad\forall\delta\mathbf{v}_{\mathrm{F}},\tag{23}$$

$$\int_{\Omega_{\mathrm{F}}}(\nabla\cdot(J_{\mathrm{A}}\mathbf{F}_{\mathrm{A}}^{-1}\mathbf{v}_{\mathrm{F}}))\delta p_{\mathrm{F}}\mathrm{d}x=0\quad\forall\delta p_{\mathrm{F}},\tag{24}$$

where $\mathrm{d}x$ indicates the integral is taken over the domain and $\mathrm{d}s$ on the boundary, and $\mathbf{v}_{\mathrm{A}}=\frac{\partial\mathbf{u}_{\mathrm{A}}}{\partial t}$ denotes the auxiliary velocity of the ALE mapping, without relation with $\mathbf{v}_{\mathrm{F}}$. Integration by parts is used in Eq. (23) to reduce the continuity requirement of $\mathbf{v}_{\mathrm{F}}$ while not in Eq. (24).

The weak form of the mesh motion model Eq. (5) with test functions $\delta\mathbf{z}_{\mathrm{A}}$, $\delta\mathbf{v}_{\mathrm{A}}$ is

$$\int_{\Omega_{\mathrm{F}}}(\mathbf{z}_{\mathrm{A}}\cdot\delta\mathbf{z}_{\mathrm{A}}-\ell(\nabla\mathbf{u}_{\mathrm{A}}):(\nabla\delta\mathbf{z}_{\mathrm{A}}))\mathrm{d}x+\int_{\partial\Omega_{\mathrm{F}}}\ell(\nabla\mathbf{u}_{\mathrm{A}})\mathbf{n}_{\mathrm{F}}\cdot\delta\mathbf{z}_{\mathrm{A}}\mathrm{d}s=0\quad\forall\delta\mathbf{z}_{\mathrm{A}},\tag{25}$$

$$\int_{\Omega_{\mathrm{F}}}\ell(\nabla\mathbf{z}_{\mathrm{A}}):(\nabla\delta\mathbf{v}_{\mathrm{A}})\mathrm{d}x-\int_{\partial\Omega_{\mathrm{F}}}\ell(\nabla\mathbf{z}_{\mathrm{A}})\mathbf{n}_{\mathrm{F}}\cdot\delta\mathbf{v}_{\mathrm{A}}\mathrm{d}s=0\quad\forall\delta\mathbf{v}_{\mathrm{A}}.\tag{26}$$

Prescribing the Dirichlet boundary condition on $\partial\Omega_{\mathrm{F}}\backslash\Gamma_{\mathrm{I}}$ for $\mathbf{u}_{\mathrm{A}}$ and accounting for Eq. (19), the boundary term in Eq. (26) will vanish. Since the fourth-order biharmonic equation is written as two equations, another boundary condition is required. It could be the Neumann boundary condition $(\nabla\mathbf{u}_{\mathrm{A}})\mathbf{n}_{\mathrm{F}}=\mathbf{0}$ on $\partial\Omega_{\mathrm{F}}$, and thus the boundary term in Eq. (25) will also vanish.

3.1.2. Continuum solid

Assuming Dirichlet boundary conditions on $\partial\Omega_{\mathrm{S}}\backslash\Gamma_{\mathrm{I}}$ and multiplying with the test function $\delta\mathbf{v}_{\mathrm{S}}$, the weak form of the continuum solid model Eq. (6) is

$$\int_{\Omega_{\mathrm{S}}}(\rho_{\mathrm{S}}\frac{\partial^2\mathbf{u}_{\mathrm{S}}}{\partial t^2}\cdot\delta\mathbf{v}_{\mathrm{S}}+\mathbf{F}_{\mathrm{S}}\mathbf{S}_{\mathrm{S}}:(\nabla\delta\mathbf{v}_{\mathrm{S}}))\mathrm{d}x-\int_{\Gamma_{\mathrm{I}}}\mathbf{F}_{\mathrm{S}}\mathbf{S}_{\mathrm{S}}\mathbf{n}_{\mathrm{S}}\cdot\delta\mathbf{v}_{\mathrm{S}}\mathrm{d}s=0\quad\forall\delta\mathbf{v}_{\mathrm{S}}.\tag{27}$$

3.1.3. Elastic beam

For the beam model Eq. (9), the weak form on the reference domain Ω_{S} $(=\Gamma_{\mathrm{I}})$ with test function $\delta\mathbf{d}_{\mathrm{S},t}=[\delta u_t,\delta w_t,\delta\psi_t]^{\mathrm{T}}$ is

$$\int_{\Omega_{\mathrm{S}}}(\rho_{\mathrm{S}}\mathbf{G}_{\mathrm{S}}\frac{\partial^2\mathbf{d}_{\mathrm{S}}}{\partial t^2}\cdot\delta\mathbf{d}_{\mathrm{S},t}+\mathbf{s}_{\mathrm{S}}\cdot\delta\mathbf{e}_{\mathrm{S},t})\mathrm{d}x-\int_{\Gamma_{\mathrm{I}}}\mathbf{f}_{\mathrm{F}}\cdot\delta\mathbf{v}_{\mathrm{S}}\mathrm{d}s=0\quad\forall\delta\mathbf{d}_{\mathrm{S},t}.\tag{28}$$

In Eq. (28), the test function for the beam internal force $\mathbf{s}_{\mathrm{S}}$ is $\delta\mathbf{e}_{\mathrm{S},t}=[\delta(\frac{\partial\varepsilon}{\partial t}),\delta(\frac{\partial\tau}{\partial t}),\delta(\frac{\partial\kappa}{\partial t})]^{\mathrm{T}}=[\delta\varepsilon_t,\delta\tau_t,\delta\kappa_t]^{\mathrm{T}}$, which can be expressed by $\delta\mathbf{d}_{\mathrm{S},t}$ using the beam kinematics Eq. (13), and the test function for the fluid force $\mathbf{f}_{\mathrm{F}}$ is $\delta\mathbf{v}_{\mathrm{S}}=[\delta u_t,\delta w_t]^{\mathrm{T}}$ (not $\delta\mathbf{d}_{\mathrm{S},t}$) since there is no bending moment component in $\mathbf{f}_{\mathrm{F}}$.

3.1.4. Thin-walled PEH

Integrating the model in Section 2.2.2 for the elastic substrate structure, the model in Section 2.3 for the piezoelectric layers, and the model in 2.4 for the electrodes and circuit, as presented in our previous work [33], we can obtain a geometrically nonlinear model for beam-like PEHs. The weak form of such an electromechanical system may be written as

$$+\int_{\Omega_{\mathrm{S}}}(\mathbf{M}_{\mathrm{PEH}}\frac{\partial^2\mathbf{d}_{\mathrm{S}}}{\partial t^2}\cdot\delta\mathbf{d}_{\mathrm{S},t}+\mathbf{s}_{\mathrm{PEH}}\cdot\delta\mathbf{e}_{\mathrm{S},t})\mathrm{d}x-\int_{\Gamma_{\mathrm{I}}}\mathbf{f}_{\mathrm{F}}\cdot\delta\mathbf{v}_{\mathrm{S}}\mathrm{d}s\tag{29a}$$

$$+\int_{\Gamma_{\mathrm{E}}}\aleph_1(\phi,\kappa)\delta\phi_t\mathrm{d}s+\int_{\Gamma_{\mathrm{E}}}\aleph_2(\phi,\kappa)\delta\kappa_t\mathrm{d}s\tag{29b}$$

$$=0\quad\forall\delta\mathbf{d}_{\mathrm{S},t},\delta\phi_t,\tag{29c}$$

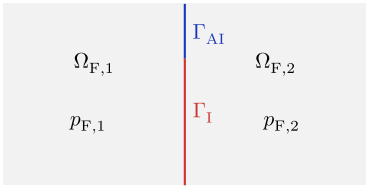


Fig. 3. Splitting domain method to account for pressure discontinuity.

where a new test function $\delta\phi_t=\delta(\frac{\partial\phi}{\partial t})$ is introduced to enforce the electrode–circuit coupling condition Eq. (18), $\aleph_1(\phi,\kappa),\aleph_2(\phi,\kappa)$ are functions describing the electric property of the PEH, and $\Gamma_{\mathrm{E}}=\Gamma_{\mathrm{I}}$ if the beam surfaces are fully covered by the electrodes. The model Eq. (29) is formulated in a manner that all variables under consideration of the laminated piezoelectric beam are condensed onto a representative line (it may not coincide with the representative line of a single-layer elastic beam), and mechanical quantities associated with this line is still denoted by the subscript $(\cdot)_{\mathrm{S}}$ since they have the same physical meaning as that of a single-layer elastic beam. In Eq. (29a), $\mathbf{M}_{\mathrm{PEH}}$ is a matrix composed of the inertial parameters of the PEH which is dependent on $\rho_{\mathrm{S}},\rho_{\mathrm{P}}$ and $\mathbf{G}_{\mathrm{S}}$ (Eq. (10)), $\mathbf{G}_{\mathrm{P}}$ (Eq. (15)). Similarly, $\mathbf{s}_{\mathrm{PEH}}$ can be expressed with a matrix describing the elastic behavior as $\mathbf{s}_{\mathrm{PEH}}=\mathbf{B}_{\mathrm{PEH}}\mathbf{e}_{\mathrm{S}}$, and $\mathbf{B}_{\mathrm{PEH}}$ also depends on the parameters of both the substrate structure and the piezoelectric layers.

3.2. Method to tackle strongly discontinuous pressure

If a thin-walled structure immersed in a flow is modeled to be non-volumetric, the different values of physical quantities through the structure thickness cannot naturally be captured using a classical continuous finite element framework because the thickness is geometrically represented by only one node. However, if this node is the common node shared by two different field variables, the values of the two variables at this node are independent of each other unless an additional coupling condition is applied. Based on this idea, we propose a simple method to tackle the strongly discontinuous pressure solution along the fluid–beam interface. As shown in Fig. 3, the fluid domain Ω_{F} is divided into two sub-domains $\Omega_{\mathrm{F},1},\Omega_{\mathrm{F},2}$ by the fluid–beam interface Γ_{I} and an artificial line Γ_{AI}, after which it is feasible to use two different variables $p_{\mathrm{F},1},p_{\mathrm{F},2}$ to represent the pressure solution over Ω_{F}. $p_{\mathrm{F},1},p_{\mathrm{F},2}$ are continuous in their respective sub-domains $\Omega_{\mathrm{F},1},\Omega_{\mathrm{F},2}$, while at the interface Γ_{I}, their values may be different because of the immersed structure. By this way, the numerical model successfully preserves the main features of the real pressure distribution of a flow surrounding a thin-walled structure. As for the values of $p_{\mathrm{F},1},p_{\mathrm{F},2}$ at Γ_{AI}, they are continuous since the pressure field is continuous in physics if no perturbation takes place at Γ_{AI}.

Remark 1. In implementation, the artificial line Γ_{AI} is necessary *only* in the construction of the function space for pressure. After meshing, Γ_{AI} naturally becomes one part of the interior boundary of the meshed domain (or the exterior boundary of the two sub-domains) and there is no need of any particular measures to eliminate this artificial line.

Remark 2. We note that the proposed splitting-domain method addresses the problem with pressure discontinuity by enabling different degrees of freedom at an interface node. It does not rely on any node manipulation (see, e.g., "node doubling" in [34,35]).

3.3. Monolithic-weak forms for coupled problems

Following the spirit of a monolithic FSI algorithm treating the fluid and solid as one surface-coupled continuum, we define the velocity $\mathbf{v}$ in the whole reference domain $\Omega=\Omega_{\mathrm{F}}\cup\Omega_{\mathrm{S}}$ as

$$\mathbf{v}=\begin{cases}\mathbf{v}_{\mathrm{F}} & \text{in}\quad\Omega_{\mathrm{F}}\\ \mathbf{v}_{\mathrm{S}} & \text{in}\quad\Omega_{\mathrm{S}}.\end{cases}\tag{30}$$

Since a boundary-fitted approach is used, the computational domains of the fluid and solid share common nodes on their interface, so with a global velocity $\mathbf{v}$, the kinematic coupling condition Eq. (20) is satisfied by construction. Furthermore, with a common test function $\delta\mathbf{v}$, the boundary term in Eq. (23) for the flow and that in Eq. (27) for the solid cancel each other due to the dynamic coupling condition Eq. (21).

The geometrical coupling condition Eq. (19) is imposed through the addition of a Lagrangian term [36] $\int_{\Gamma_\mathrm{I}} \mathbf{g}\cdot(\mathbf{v}_\mathrm{A}-\mathbf{v})\mathrm{d}s$, to which the first variation is

$$\int_{\Gamma_\mathrm{I}} ((\mathbf{v}_\mathrm{A}-\mathbf{v})\cdot\delta\mathbf{g}+\mathbf{g}\cdot(\delta\mathbf{v}_\mathrm{A}-\delta\mathbf{v}))\mathrm{d}s = 0 \quad \forall\delta\mathbf{g},\delta\mathbf{v}_\mathrm{A},\delta\mathbf{v}. \tag{31}$$

The Lagrange multiplier $\mathbf{g}$ may be regarded as a "force" which prevents the moving mesh and the structure from penetrating or separating. Eq. (31) is an alternative choice to satisfy the geometrical coupling condition other than the common method in literature, e.g., [26,27,37], where a global variable of displacement in $\Omega = \Omega_\mathrm{F}\cup\Omega_\mathrm{S}$ is defined for the mesh motion model and the structure, and thus the geometrical coupling condition is satisfied by construction. Nevertheless, the benefit of Eq. (31) is obvious: It expresses the geometrical coupling condition explicitly, and the degrees of freedom are fewer since the variable associated with the mesh motion model ($\mathbf{v}_\mathrm{A}$ in Ω_F) does not extend to Ω_S, which, further eliminates the necessity of the expression w.r.t. $\mathbf{v}_\mathrm{A}$ in Ω_S.

3.3.1. A volumetric solid coupled with a flow

We can attain the monolithic-weak form of sub-problem (I) by combining Eqs (23)–(27), (31), and it is

$$+\int_{\Omega_\mathrm{F}} (\rho_\mathrm{F} J_\mathrm{A}(\frac{\partial\mathbf{v}}{\partial t}+(\nabla\mathbf{v})\mathbf{F}_\mathrm{A}^{-1}(\mathbf{v}-\mathbf{v}_\mathrm{A}))\cdot\delta\mathbf{v} + J_\mathrm{A}\mathbf{T}_\mathrm{F}\mathbf{F}_\mathrm{A}^{-\mathrm{T}}:(\nabla\delta\mathbf{v}))\mathrm{d}x$$

$$+\int_{\Omega_\mathrm{F}} (\nabla\cdot(J_\mathrm{A}\mathbf{F}_\mathrm{A}^{-1}\mathbf{v}))\delta p_\mathrm{F}\mathrm{d}x \tag{32a}$$

$$+\int_{\Omega_\mathrm{F}} (\mathbf{z}_\mathrm{A}\cdot\delta\mathbf{z}_\mathrm{A}-\ell(\nabla\mathbf{u}_\mathrm{A}):(\nabla\delta\mathbf{z}_\mathrm{A}))\mathrm{d}x+\int_{\Omega_\mathrm{F}}\ell(\nabla\mathbf{z}_\mathrm{A}):(\nabla\delta\mathbf{v}_\mathrm{A})\mathrm{d}x \tag{32b}$$

$$+\int_{\Omega_\mathrm{S}} (\rho_\mathrm{S}\frac{\partial^2\mathbf{u}_\mathrm{S}}{\partial t^2}\cdot\delta\mathbf{v}+\mathbf{F}_\mathrm{S}\mathbf{S}_\mathrm{S}:(\nabla\delta\mathbf{v}))\mathrm{d}x \tag{32c}$$

$$+\int_{\Gamma_\mathrm{I}} ((\mathbf{v}_\mathrm{A}-\mathbf{v})\cdot\delta\mathbf{g}+\mathbf{g}\cdot(\delta\mathbf{v}_\mathrm{A}-\delta\mathbf{v}))\mathrm{d}s \tag{32d}$$

$$=0 \quad \forall\delta\mathbf{v}_\mathrm{A},\delta\mathbf{v},\delta p_\mathrm{F},\delta\mathbf{z}_\mathrm{A},\delta\mathbf{g}. \tag{32e}$$

It is clear that Eq. (32) includes five primary unknowns to be solved: auxiliary velocity $\mathbf{v}_\mathrm{A}$ of the fluid mesh in Ω_F, global velocity for the flow and solid $\mathbf{v}$ in Ω, fluid pressure p_F in Ω_F, intermediate mesh variable $\mathbf{z}_\mathrm{A}$ in Ω_F, and Lagrange multiplier $\mathbf{g}$ on Γ_I. Other variables present in Eq. (32) such as $\mathbf{u}_\mathrm{A},\mathbf{u}_\mathrm{S}$ can be expressed by the above primary unknowns using an appropriate time integration scheme, which is discussed later on in Section 3.4.

3.3.2. A non-volumetric beam coupled with a flow

Similarly, combining Eqs. (23)–(26), (28), (31) with the method in Section 3.2 to account for the pressure discontinuity, the monolithic-weak form of sub-problem (II) is stated as

$$+\sum_{j=1}^{2}\int_{\Omega_j} (\rho_\mathrm{F} J_\mathrm{A}(\frac{\partial\mathbf{v}}{\partial t}+(\nabla\mathbf{v})\mathbf{F}_\mathrm{A}^{-1}(\mathbf{v}-\mathbf{v}_\mathrm{A}))\cdot\delta\mathbf{v} + J_\mathrm{A}\mathbf{T}_{\mathrm{F},j}\mathbf{F}_\mathrm{A}^{-\mathrm{T}}:(\nabla\delta\mathbf{v}))\mathrm{d}x$$

$$+\sum_{j=1}^{2}\int_{\Omega_j} (\nabla\cdot(J_\mathrm{A}\mathbf{F}_\mathrm{A}^{-1}\mathbf{v}))\delta p_{\mathrm{F},j}\mathrm{d}x \tag{33a}$$

$$+\sum_{j=1}^{2}\int_{\Omega_j} (\mathbf{z}_\mathrm{A}\cdot\delta\mathbf{z}_\mathrm{A}-\ell(\nabla\mathbf{u}_\mathrm{A}):(\nabla\delta\mathbf{z}_\mathrm{A}))\mathrm{d}x+\sum_{j=1}^{2}\int_{\Omega_j}\ell(\nabla\mathbf{z}_\mathrm{A}):(\nabla\delta\mathbf{v}_\mathrm{A})\mathrm{d}x \tag{33b}$$

$$+\int_{\Gamma_\mathrm{I}} (\rho_\mathrm{S}\mathbf{G}_\mathrm{S}\frac{\partial^2\mathbf{d}_\mathrm{S}}{\partial t^2}\cdot\delta\mathbf{d}_{\mathrm{S},t}+\mathbf{s}_\mathrm{S}\cdot\delta\mathbf{e}_{\mathrm{S},t})\mathrm{d}s \tag{33c}$$

$$+\int_{\Gamma_\mathrm{I}} ((\mathbf{v}_\mathrm{A}-\mathbf{v})\cdot\delta\mathbf{g}+\mathbf{g}\cdot(\delta\mathbf{v}_\mathrm{A}-\delta\mathbf{v}))\mathrm{d}s \tag{33d}$$

$$=0 \quad \forall\delta\mathbf{v}_\mathrm{A},\delta\mathbf{v},\delta\psi_t,\delta p_{\mathrm{F},1},\delta p_{\mathrm{F},2},\delta\mathbf{z}_\mathrm{A},\delta\mathbf{g}. \tag{33e}$$

For sub-problem (II), $\Omega_\mathrm{F}=\Omega$ and $\Omega_\mathrm{S}=\Gamma_\mathrm{I}$, so in line (33a), (33b), $\Omega_{\mathrm{F},j}$ is simplified to be Ω_j, and in line (33c), Ω_S is replaced by Γ_I. In line (33a), the subscript $(\cdot)_j$ shows for the stress $\mathbf{T}_\mathrm{F}$ because $\mathbf{T}_\mathrm{F}$ is dependent on the pressure p_F, as seen in Eq. (3). Except for the five unknowns present also in sub-problem (I), two other unknowns, i.e., the time rate of beam cross-section rotation ψ_t and an additional fluid pressure field $p_{\mathrm{F},1}$ or $p_{\mathrm{F},2}$ have to be solved for sub-problem (II). Exactly the same as $\mathbf{u}_\mathrm{A},\mathbf{u}_\mathrm{S}$, the beam cross-section rotation ψ is also computed by the time integration scheme.

3.3.3. A non-volumetric PEH coupled with a flow

The monolithic-weak form of sub-problem (III) is obtained by substituting line (33c) with the weak form of a thin-walled PEH Eq. (29):

$$+\sum_{j=1}^{2}\int_{\Omega_j} (\rho_\mathrm{F} J_\mathrm{A}(\frac{\partial\mathbf{v}}{\partial t}+(\nabla\mathbf{v})\mathbf{F}_\mathrm{A}^{-1}(\mathbf{v}-\mathbf{v}_\mathrm{A}))\cdot\delta\mathbf{v} + J_\mathrm{A}\mathbf{T}_{\mathrm{F},j}\mathbf{F}_\mathrm{A}^{-\mathrm{T}}:(\nabla\delta\mathbf{v}))\mathrm{d}x$$

$$+\sum_{j=1}^{2}\int_{\Omega_j} (\nabla\cdot(J_\mathrm{A}\mathbf{F}_\mathrm{A}^{-1}\mathbf{v}))\delta p_{\mathrm{F},j}\mathrm{d}x \tag{34a}$$

$$+\sum_{j=1}^{2}\int_{\Omega_j} (\mathbf{z}_\mathrm{A}\cdot\delta\mathbf{z}_\mathrm{A}-\ell(\nabla\mathbf{u}_\mathrm{A}):(\nabla\delta\mathbf{z}_\mathrm{A}))\mathrm{d}x+\sum_{j=1}^{2}\int_{\Omega_j}\ell(\nabla\mathbf{z}_\mathrm{A}):(\nabla\delta\mathbf{v}_\mathrm{A})\mathrm{d}x \tag{34b}$$

$$+\int_{\Gamma_\mathrm{I}} (\mathbf{M}_\mathrm{PEH}\frac{\partial^2\mathbf{d}_\mathrm{S}}{\partial t^2}\cdot\delta\mathbf{d}_{\mathrm{S},t}+\mathbf{s}_\mathrm{PEH}\cdot\delta\mathbf{e}_{\mathrm{S},t})\mathrm{d}s \tag{34c}$$

$$+\int_{\Gamma_\mathrm{E}} \aleph_1(\phi,\kappa)\delta\phi_t\mathrm{d}s+\int_{\Gamma_\mathrm{E}}\aleph_2(\phi,\kappa)\delta\kappa_t\mathrm{d}s \tag{34d}$$

$$+\int_{\Gamma_\mathrm{I}} ((\mathbf{v}_\mathrm{A}-\mathbf{v})\cdot\delta\mathbf{g}+\mathbf{g}\cdot(\delta\mathbf{v}_\mathrm{A}-\delta\mathbf{v}))\mathrm{d}s \tag{34e}$$

$$=0 \quad \forall\delta\mathbf{v}_\mathrm{A},\delta\mathbf{v},\delta\psi_t,\delta\phi_t,\delta p_{\mathrm{F},1},\delta p_{\mathrm{F},2},\delta\mathbf{z}_\mathrm{A},\delta\mathbf{g}, \tag{34f}$$

where one more unknown is involved if compared with sub-problem (II), i.e., the time rate of the PEH voltage output ϕ_t, so finally, for a thin-walled PEH immersed in a flow, we need to solve for eight unknowns.

3.4. Time integration scheme

The monolithic-weak forms presented in Section 3.3 are ready to be discretized in finite dimensional sub-spaces. The obtained semi-discrete equations are then able to be solved with the help of an appropriate time integration scheme. In this work, we use the generalized-α method, which is proposed by [38] for structural dynamics and extended by [39] to fluid dynamics. This method is also used for FSI problems such as [40,41], but some special issues should be noted in such cases, particularly when working with a monolithic coupling algorithm, since structural dynamics equation is second-order differential w.r.t. time (Eq. (6)), while fluid dynamics equation is first-order differential w.r.t. time (Eq. (1)).

In what follows, the computational time interval $[0,T]$ is subdivided into time instants $0=t_0<t_1<t_2\cdots<t_N=T$ with time increment $\Delta t=t_{n+1}-t_n, n=0,1,2,\ldots,N-1$; variables already known at t_n are denoted with the superscript $(\cdot)^n$ and variables to be solved at the next time step with $(\cdot)^{n+1}$; first-order differential w.r.t. time is indicated by the subscript $(\cdot)_{\mathrm{dif}}$ and single integral w.r.t. time by $(\cdot)_{\mathrm{int}}$.

3.4.1. Generalized-α method for fluid dynamics

For fluid dynamics, we choose the velocity as the primary unknown U. The fluid acceleration at time instant t_{n+1} is then given by [39]

$$U_{\mathrm{dif}}^{n+1}=\frac{1}{\gamma^\mathrm{F}\Delta t}(U^{n+1}-U^n)+\frac{\gamma^\mathrm{F}-1}{\gamma^\mathrm{F}}U_{\mathrm{dif}}^n, \tag{35}$$

where γ^{F} is a free parameter at this point. To achieve a second-order accurate and unconditionally stable method, the following equations are finally used to update the semi-discrete system of interest [39]:

$$U^{n+\alpha_f^{\mathrm{F}}} = U^n + \alpha_f^{\mathrm{F}}(U^{n+1} - U^n), \tag{36}$$

$$U_{\mathrm{dif}}^{n+\alpha_m^{\mathrm{F}}} = U_{\mathrm{dif}}^n + \alpha_m^{\mathrm{F}}(U_{\mathrm{dif}}^{n+1} - U_{\mathrm{dif}}^n). \tag{37}$$

Eq. (36) is also employed to update the fluid pressure field. Parameters $\alpha_m^{\mathrm{F}}, \alpha_f^{\mathrm{F}}, \gamma^{\mathrm{F}}$ are expressed using the spectral radius $\rho_\infty^{\mathrm{F}} \in [0,1]$ that specifies high frequency damping

$$\alpha_m^{\mathrm{F}} = \frac{1}{2}\left(\frac{3-\rho_\infty^{\mathrm{F}}}{1+\rho_\infty^{\mathrm{F}}}\right), \quad \alpha_f^{\mathrm{F}} = \frac{1}{1+\rho_\infty^{\mathrm{F}}}, \quad \gamma^{\mathrm{F}} = \frac{1}{2} + \alpha_m^{\mathrm{F}} - \alpha_f^{\mathrm{F}}. \tag{38}$$

3.4.2. Generalized-α method for structural dynamics

For the structural dynamics, we also choose the velocity and time rate quantities (e.g., ψ_t, ϕ_t) as the primary unknown U. The acceleration and (equivalent) displacement as well as the velocity are then updated by [38]

$$U_{\mathrm{dif}}^{n+1} = \frac{(\gamma^{\mathrm{S}}-1)}{\gamma^{\mathrm{S}}} U_{\mathrm{dif}}^n + \frac{1}{\Delta t \gamma^{\mathrm{S}}}(U^{n+1} - U^n), \tag{39}$$

$$U_{\mathrm{int}}^{n+1} = U_{\mathrm{int}}^n + \frac{\Delta t(\gamma^{\mathrm{S}} - \beta^{\mathrm{S}})}{\gamma^{\mathrm{S}}} U^n + \frac{\Delta t^2(\gamma^{\mathrm{S}} - 2\beta^{\mathrm{S}})}{2\gamma^{\mathrm{S}}} U_{\mathrm{dif}}^n + \frac{\Delta t \beta^{\mathrm{S}}}{\gamma^{\mathrm{S}}} U^{n+1}, \tag{40}$$

$$U_{\mathrm{dif}}^{n+\alpha_m^{\mathrm{S}}} = U_{\mathrm{dif}}^n + \alpha_m^{\mathrm{S}}(U_{\mathrm{dif}}^{n+1} - U_{\mathrm{dif}}^n), \tag{41}$$

$$U_{\mathrm{int}}^{n+\alpha_f^{\mathrm{S}}} = U_{\mathrm{int}}^n + \alpha_f^{\mathrm{S}}(U_{\mathrm{int}}^{n+1} - U_{\mathrm{int}}^n), \tag{42}$$

$$U^{n+\alpha_f^{\mathrm{S}}} = U^n + \alpha_f^{\mathrm{S}}(U^{n+1} - U^n). \tag{43}$$

Parameters $\alpha_f^{\mathrm{S}}, \alpha_m^{\mathrm{S}}, \gamma^{\mathrm{S}}$ are still used to realize second-order accuracy and unconditional stability, given with the spectral radius $\rho_\infty^{\mathrm{S}} \in [0,1]$ by [38]

$$\alpha_m^{\mathrm{S}} = \frac{2-\rho_\infty^{\mathrm{S}}}{1+\rho_\infty^{\mathrm{S}}}, \quad \alpha_f^{\mathrm{S}} = \frac{1}{1+\rho_\infty^{\mathrm{S}}}, \quad \gamma^{\mathrm{S}} = \frac{1}{2} + \alpha_m^{\mathrm{S}} - \alpha_f^{\mathrm{S}}, \quad \beta^{\mathrm{S}} = \frac{1}{4}(1 + \alpha_m^{\mathrm{S}} - \alpha_f^{\mathrm{S}})^2. \tag{44}$$

3.4.3. Generalized-α method for monolithic FSI

We note that for the FSI problems present in Section 3.3, four more variables in addition to that mentioned in Sections 3.4.1 and 3.4.2, need to be updated, i.e., the auxiliary displacement $\mathbf{u}_{\mathrm{A}}$, auxiliary velocity $\mathbf{v}_{\mathrm{A}}$, mesh intermediate variable $\mathbf{z}_{\mathrm{A}}$, and Lagrange multiplier $\mathbf{g}$. $\mathbf{u}_{\mathrm{A}}$ is updated using Eq. (42) since no formulation is available to update the displacement in Section 3.4.1, and thus it is natural to use Eq. (43) rather than Eq. (36) to update $\mathbf{v}_{\mathrm{A}}$ and $\mathbf{z}_{\mathrm{A}}$; $\mathbf{g}$ is updated also with Eq. (43).

Considering the kinematic and dynamic coupling conditions Eqs. (20)–(21), the fluid and solid velocity should be evaluated at the same time instant, otherwise the overall FSI scheme will be less stable and less accurate [42]. This requirement renders $\alpha_f^{\mathrm{F}} = \alpha_f^{\mathrm{S}}$ if comparing Eq. (36) with Eq. (43), thus $\rho_\infty^{\mathrm{F}} = \rho_\infty^{\mathrm{S}}$. Further more, since we work with a monolithic algorithm, we need to evaluate the fluid and solid acceleration also at the same time instant, which necessities $\alpha_m^{\mathrm{F}} = \alpha_m^{\mathrm{S}}$. If both $\rho_\infty^{\mathrm{F}} = \rho_\infty^{\mathrm{S}}$ and $\alpha_m^{\mathrm{F}} = \alpha_m^{\mathrm{S}}$ are satisfied, $\rho_\infty^{\mathrm{F}} = \rho_\infty^{\mathrm{S}} = 1$ will be the only choice. However, $\rho_\infty^{\mathrm{F}} = \rho_\infty^{\mathrm{S}} = 1$ means no high frequency damping is introduced, resulting in an insufficiently robust numerical scheme in practice. This issue may be alleviated by selecting an appropriate ρ_∞^{F} and determining both the fluid and solid parameters $\alpha_m^{\mathrm{F}}, \alpha_f^{\mathrm{F}}, \alpha_m^{\mathrm{S}}, \alpha_f^{\mathrm{S}}$ using Eq. (38). By this way, the fluid sub-problem is always optimally damped, and the time integration scheme for the solid sub-problem remains second-order accurate and unconditionally stable since the expressions for $\gamma^{\mathrm{S}}, \beta^{\mathrm{S}}$ in Eq. (44) still hold [40].

3.5. Solution algorithm

With space discretization using the Galerkin method (same trial and test function space for a variable) and time integration using the above generalized-α method, we obtain a nonlinear algebraic set of equations given by

$$\boldsymbol{\mathcal{S}}(\mathbf{x}) = \mathbf{0}, \tag{45}$$

where $\boldsymbol{\mathcal{S}}$ represents the coupled system Eq. (32), Eq. (33) or Eq. (34) after spatial and temporal discretization, and $\mathbf{x}$ is the corresponding primary unknowns. The Newton–Raphson (N-R) method [43] is used to solve Eq. (45): in each time step, the following linear equation is solved iteratively

$$\mathbf{x}^1 = \mathbf{x}^0 - \frac{\boldsymbol{\mathcal{S}}(\mathbf{x}^0)}{\boldsymbol{\mathcal{S}}'(\mathbf{x}^0)}, \tag{46}$$

where $\mathbf{x}^0$ and $\mathbf{x}^1$ are the solution in the current and the next iteration step, respectively, $\boldsymbol{\mathcal{S}}'(\mathbf{x}^0) = \frac{\partial \boldsymbol{\mathcal{S}}}{\partial \mathbf{x}}(\mathbf{x}^0)$, until the difference between $\mathbf{x}^0$ and $\mathbf{x}^1$ smaller than the given tolerance criterion.

4. Model validation: two FSI benchmark problems

In this section, we implement two popular benchmark problems in the FSI community to validate the monolithic solution scheme proposed in Section 3. We restrict to two dimensions (2D) to decrease the computational cost. The continuum solid model in Section 2.2.1 is reduced to a 2D problem using the plane strain assumption. The beam in Section 2.2.2 thus becomes a plate with the unit width $b_{\mathrm{S}} = 1$ m, and considering the beam model is derived using the plane stress assumption, we modify the beam bending stiffness by multiplying with a coefficient $1/(1-\nu_{\mathrm{S}}^2)$ to make it consistent with the continuum solid model. Finite element function spaces chosen for the primary unknowns $\mathbf{v}_{\mathrm{A}}, \mathbf{v}, p_{\mathrm{F}}$ (or $p_{\mathrm{F},1}, p_{\mathrm{F},2}$), $\psi_t, \mathbf{z}_{\mathrm{A}}, \mathbf{g}$ are Lagrange $P2, P2, P1, P1, P2, P2$. With this choice, stable discretization of the fluid field is achieved using Taylor–Hood $P2/P1$ elements [44], and shear-locking effects are avoid for the beam model [45]. All simulations are performed using the open-source computing platform FEniCS [46] and the extension Multiphenics. FEniCS can discretize mathematical models and generate efficient finite element code. To solve the nonlinear weak form with the N-R method, the automatic functional differentiation (AD) in the Unified Form Language (UFL) is employed. The resulting monolithic system of algebraic equations within each Newton's step can be solved with a variety of techniques available through the linear algebra backend PETSc [47]. A parallel direct solver (MUMPS [48]) is used in the following numerical examples, where the degrees of freedom are between 1×10^5 and 2×10^5. If the problem size is larger, preconditioning may be required, e.g., to simplify the Jacobian in the N-R method by neglecting all derivatives w.r.t. the ALE deformation [49]. The convergence of simulation results w.r.t. the number of finite elements and time step size is examined for every example.

4.1. Benchmark 1: a flexible structure attached to a rigid cylinder in a flow

4.1.1. Problem setup

This problem is the FSI2 benchmark taken from [50]. The geometrical configuration and boundary conditions are shown in Fig. 4, where the velocity profile in x-direction at Γ_{in} is

$$v_x = \begin{cases} 1.5\frac{4y(0.41-y)}{0.41^2}\frac{1-\cos(0.5\pi t)}{2}, & \text{if} \quad t < 2 \\ 1.5\frac{4y(0.41-y)}{0.41^2}, & \text{otherwise.} \end{cases} \tag{47}$$

The left end of the elastic structure is attached to the fixed cylinder, with the length of 0.35 m and thickness of 0.02 m. Point A $(0.6, 0.2)$ is the center of the structure free end, which serves as a control point for the numerical validation. Material parameters are: $\rho_{\mathrm{F}} = 10^3$ kgm^{-3}, $\mu_{\mathrm{F}} = 1$ kg(ms)$^{-1}$; $\rho_{\mathrm{S}} = 10^4$ kgm^{-3}, $\mu_{\mathrm{S}} = 5\times10^5$ Pa, $\nu_{\mathrm{S}} = 0.4$. The Reynolds number of this setup is 100. After the flow is fully developed, the

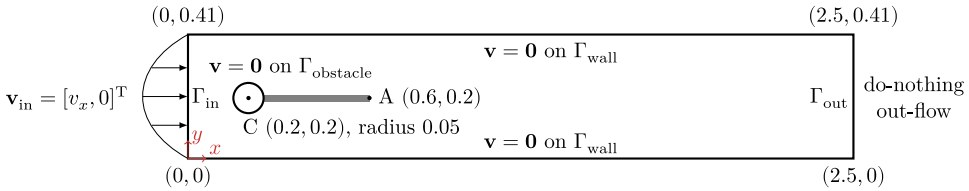
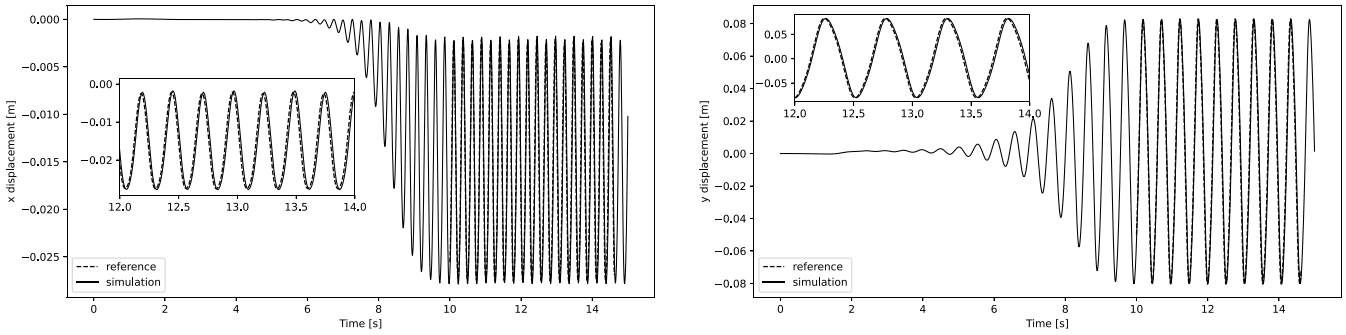


Fig. 4. Geometrical configuration and boundary conditions of the FSI benchmark 1, length unit [m].



(a) Displacement of point A in x-direction

(b) Displacement of point A in y-direction

Fig. 5. Comparison of the displacements at point A obtained by solution of Eq. (32) and the reference data, benchmark 1.

flexible structure will maintain vortex-induced periodic oscillations at a constant magnitude. In addition to the physical boundary conditions described above, we prescribe no-slip condition on $\Gamma_{\text{in}} \cup \Gamma_{\text{out}} \cup \Gamma_{\text{obstacle}} \cup \Gamma_{\text{wall}}$ for the moving mesh.

4.1.2. Numerical results when using the volumetric solid

In this part, we compare the displacement of point A $(0.6, 0.2)$ and lift force around the cylinder and the flexible structure (flag) obtained by solving Eq. (32) with reference data available here, as shown in Fig. 5 and Fig. 6. The computational time interval is [0 s, 15 s], and the time step size is 0.01 s. The number of the mesh elements N_{elem} is 9496, and the number of the degrees of freedom N_{dof} is 106641. The tolerance criterion for the N-R method is set to be 1×10^{-8}. It is clear to see from Figs. 5–6 that all quantities in the comparison are in good agreement. For instance, the reference values for the x and y displacement given by [50] are $(-1.458 \pm 1.244) \times 10^{-2}$ m, $(0.123 \pm 8.06) \times 10^{-2}$ m, respectively; in our simulation, the two values are $(-1.479 \pm 1.301) \times 10^{-2}$ m and $(0.125 \pm 8.125) \times 10^{-2}$ m, so the relative error between the y displacement is approximately 0.8%.

The artificial material parameter of the moving mesh is $\ell = 0.01$ Pa. In principle, the value of ℓ does not influence the physical solution as long as the associated ALE mapping is well realized. However, for the monolithic-weak form proposed in this work, the moving mesh equation Eq. (26) shares a common test function $\delta \mathbf{v}_{\text{A}}$ with the geometrical coupling condition Eq. (31), meaning that the moving mesh is not completely non-physical, so the value of ℓ should be carefully determined. The method is to choose an adequately small ℓ that ensures the physical solution not sensitive to ℓ when ℓ is smaller, but apparently, ℓ cannot be extremely small since the mesh equation should play a role in the coupled system. The value of the spectral radius ρ_{∞}^{F} for the time integration scheme does not affect the simulation result, but the computation becomes not robust if without numerical damping. As seen in the sub-figure of Fig. 6, when $\rho_{\infty}^{\text{F}} = 1$, the curve of the lift force on the flag is not smooth after 13 s, whereas when $\rho_{\infty}^{\text{F}} = 0.9$, a smooth curve for the lift force over the computational time is achieved. It seems that at about 10 s, the curve of the reference data is not smooth, too. The reason could be also relevant to the numerical damping of the time integration scheme, which is however, not mentioned in the original reference paper [50].

4.1.3. Numerical results when using the non-volumetric beam

This part is devoted to the numerical results of sub-problem (II), where the structure is modeled as a non-volumetric beam. The comparison is between Eq. (32) and Eq. (33) since Eq. (32) has been well validated in Section 4.1.2. The same mesh with $N_{\text{elem}} = 9496$ is used in this simulation, but for Eq. (33), $N_{\text{dof}} = 121094$, a bit larger than that for Eq. (32). Except for the displacement (Fig. 7) and lift force (Fig. 8), the pressure distribution at several time instants is also given to show that Eq. (33) is capable of capturing the strong discontinuity of the pressure solution, as seen in Fig . 9.

Fig. 7 shows that the displacement predicted by Eq. (33) is slightly larger than that by Eq. (32). If taking the y displacement obtained from Eq. (32) as the reference, the relative error is approximately 10% (for Eq. (33), y displacement is $(0.118 \pm 8.936) \times 10^{-2}$ m). This prediction is consistent with Fig. 8, where the lift force on the flag and the cylinder is presented. The lift on the flag when using the beam model is evaluated along a path that coincides with the real structure shape. Eq. (33) predicts also a bit higher lift on the flag, but the lift on the cylinder is the same, which implies that splitting the fluid domain does not impair the accuracy of computational results. Therefore, the discrepancy between the results of Eq. (33) and Eq. (32) may originate from the geometry change of the flag in the two structural model. Actually, the flexible structure in this benchmark problem is not very thin (the thickness-to-length ratio is 5.7%), so there exists non-negligible effects of weakly discontinuous velocity gradient along the fluid–solid interface, which, nevertheless, is not accounted for in Eq. (33). At this point, we may postulate that if the flexible structure is adequately thin, Eq. (33) will predict results much more similar to that of Eq. (32). This postulation is demonstrated in the second benchmark problem.

4.2. Benchmark 2: a flexible structure attached to a rigid square in a flow

4.2.1. Problem setup

This benchmark has been reported widely in literature. Fig. 10 shows the problem setting re-sketched based on [41]. The center of the rigid square is fixed at point C $(0.05, 0.06)$, and the free end of the flexible structure is at point A $(0.095, 0.06)$. They are initially immersed in a uniform flow with $v_{\infty} = 0.513$ ms^{-1}. The structure length is 0.04 m and the thickness is 0.0006 m. Material parameters are: $\rho_{\text{F}} = 1.18$ kgm^{-3}, $\mu_{\text{F}} = 1.82 \times 10^{-5}$ kg(ms)$^{-1}$; $\rho_{\text{S}} = 10^2$ kgm^{-3}, $c_{\text{S}} = 2.5 \times 10^5$

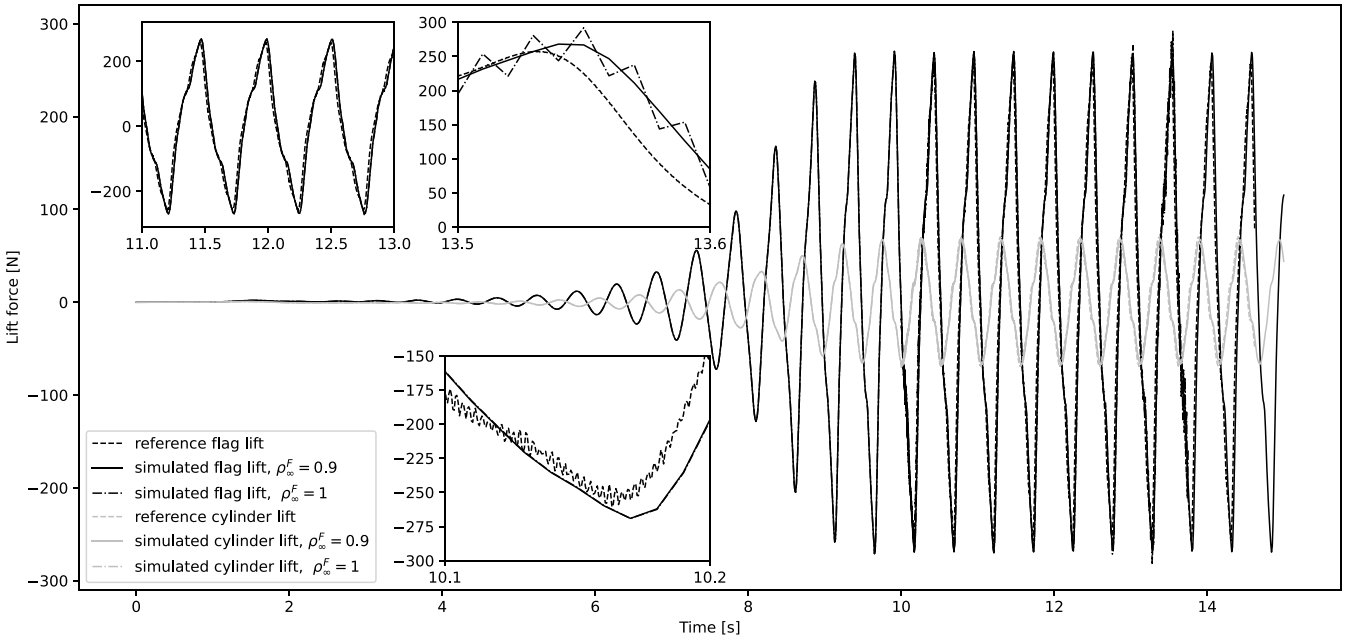
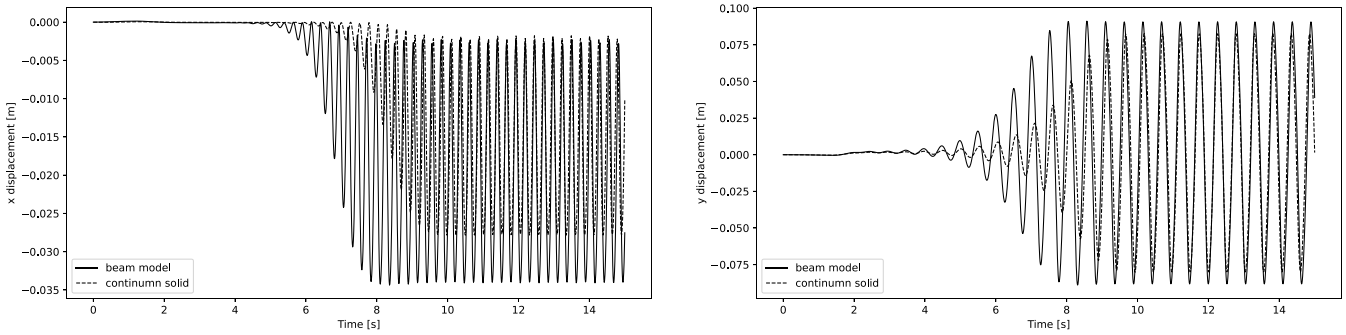


Fig. 6. Comparison of the lift force obtained from the solution of Eq. (32) and the reference data, benchmark 1.



(a) Displacement of point A in x-direction

(b) Displacement of point A in y-direction

Fig. 7. Comparison of the displacement at point A obtained by solution of Eqs. (32) and (33), benchmark 1.

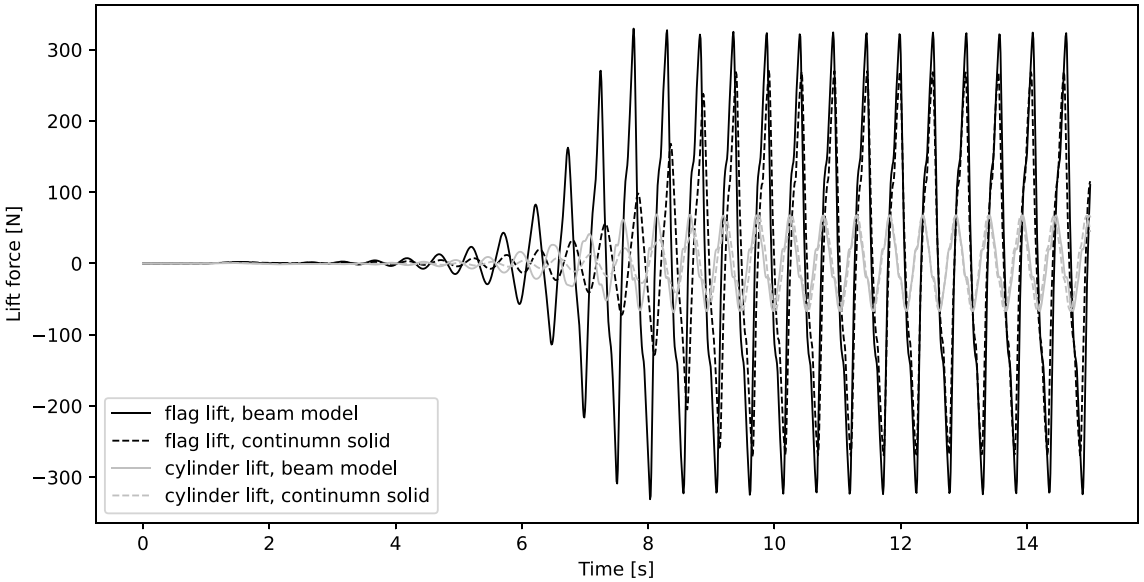


Fig. 8. Comparison of the lift force obtained from solution of Eqs. (32) and (33), benchmark 1.



(a) Pressure distribution at $t = 4$ s



(b) Pressure distribution at $t = 8$ s



(c) Pressure distribution at $t = 12$ s



(d) Pressure distribution at $t = 15$ s

Fig. 9. Pressure distribution at different time instants, benchmark 1.

Pa, $\nu_S = 0.35$. The Reynolds number of this setup is approximately 333. The boundary conditions for the moving mesh are the same as that in Section 4.1.1.

4.2.2. Numerical results for solid/beam model

For this benchmark, the computational time interval is [0 s, 12 s], the time step size is $\Delta t = 0.006$ s, the artificial material parameter of the moving mesh is $\ell = 0.001$ Pa, and the spectral radius is $\rho_\infty^{\mathrm{F}} = 0.7$. The same mesh with $N_{\mathrm{elem}} = 13536$ is used for the two simulations, and $N_{\mathrm{dof}} = 169728$ for Eq. (32) while $N_{\mathrm{dof}} = 171450$ for Eq. (33). The tolerance criterion for the N-R method is 5×10^{-8}. The displacement of the control point A is shown in Fig. 11, and as before, the pressure distribution at different time instants obtained from Eq. (33) is also presented (Fig. 12). It can be seen that for this thin structure (the thickness-to-length ratio is 1.5%), no significant difference in the long-term response is observed between the results of the two simulations.

According to Table 2 of paper [13], which summarizes the numerical results of this problem available from eight papers (all using a partitioned coupling algorithm), the oscillating frequency of the flexible structure and its maximum tip displacement in y-direction are in the range [2.77 Hz, 3.25 Hz] and [0.0095 m, 0.014 m], respectively. In our simulation, the frequency is approximately 3.25 Hz, and the transverse vibration magnitude (Fig. 11(b)) obviously drops to the above range. Therefore, the monolithic solution scheme given by Eq. (32) and Eq. (33) are well validated against this benchmark problem.

5. Numerical examples of flow-driven PEHs

In the preceding section, the monolithic solution scheme developed for a classical FSI setting (sub-problem (I), Eq. (32)) and for a special case where a non-volumetric representation is employed for the solid (sub-problem (II), Eq. (33)) has been validated via numerical experiments. In this section, we consider sub-problem (III), i.e., a beam-like

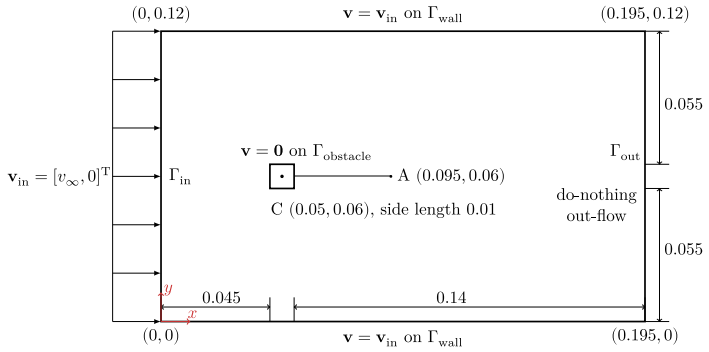
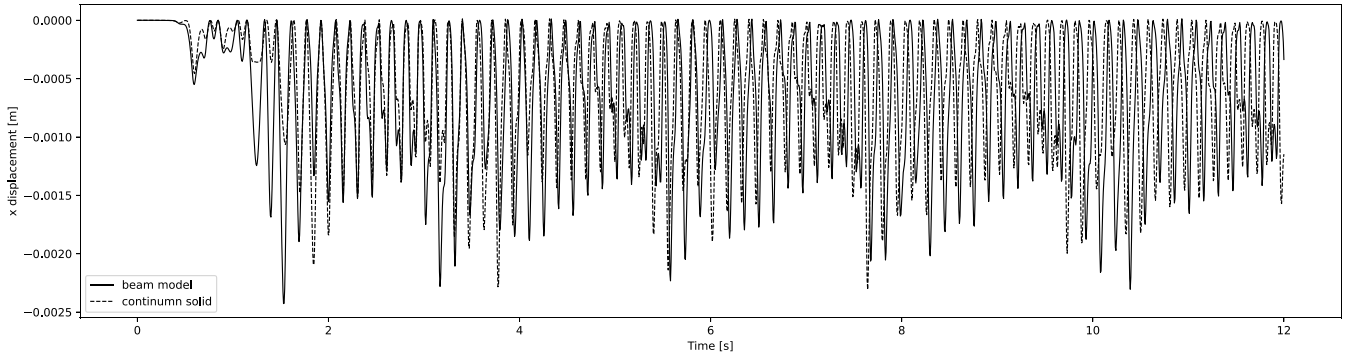
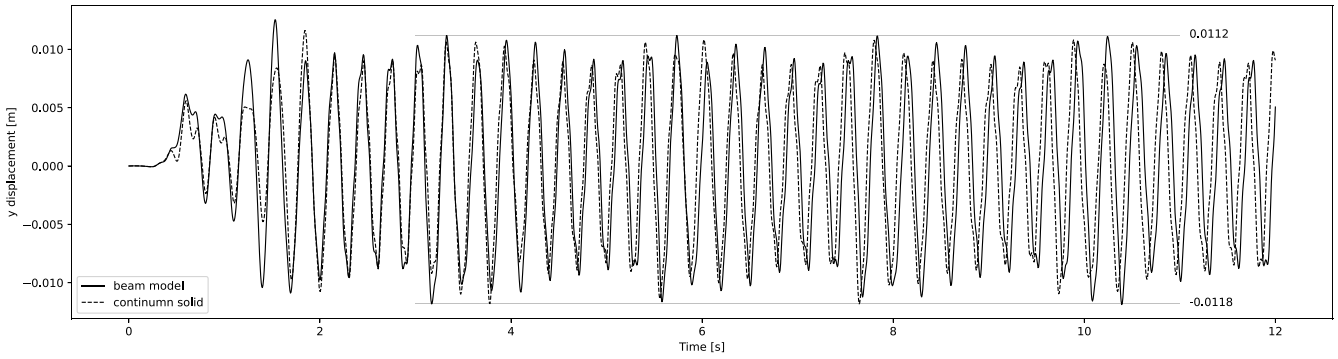


Fig. 10. Geometrical configuration and boundary conditions of the FSI benchmark 2, length unit [m].



(a) Displacement of point A in x-direction



(b) Displacement of point A in y-direction

Fig. 11. Comparison of the displacement at point A between Eqs. (32) and (33), benchmark 2.

PEH driven by a flow, given by Eq. (34). Extension from sub-problem (II) to sub-problem (III) is straightforward, with only two revisions: (1) as seen in Eq. (34c), the matrices associated with the inertial parameters and the elastic parameters need to be tailored for a PEH, and (2) the voltage-related equation Eq. (34d) should be incorporated. This method is illustrated in what follows by two numerical examples, both taking a symmetric bimorph that bears a parallel-connection circuit and is fully covered by the electrodes (a PEH in this configuration is shown in Fig. 1) to harvest flow energy. The two examples manifest that the proposed framework is feasible to investigate thin-walled PEHs immersed in fluid.

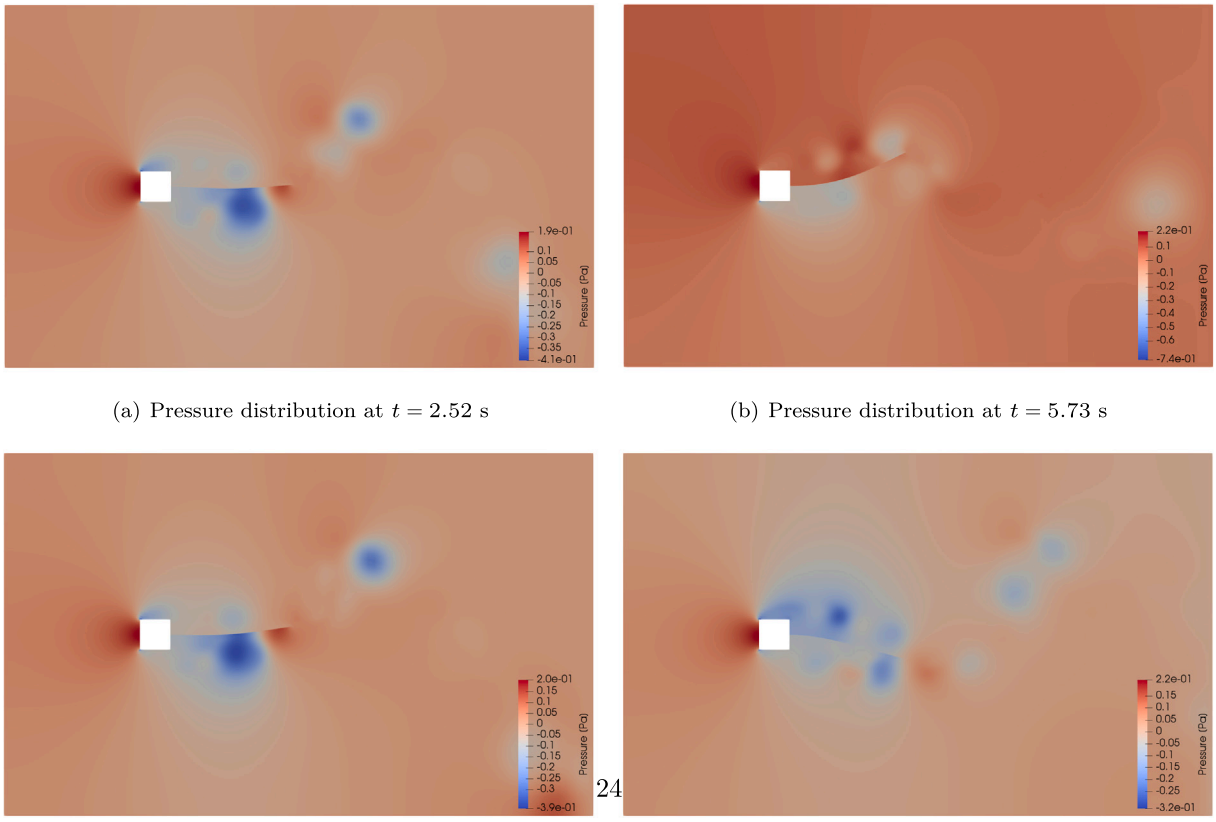
5.1. PEH specific equations

With reference to our previous work [33], for a PEH in the aforementioned configuration, the matrices to describe its inertial and elastic behavior are

$$\mathbf{M}_{\mathrm{PEH}} = \begin{bmatrix} \rho_{\mathrm{S}} b_{\mathrm{S}} h_{\mathrm{S}} + 2\rho_{\mathrm{P}} b_{\mathrm{P}} h_{\mathrm{P}} & 0 & 0 \\ 0 & \rho_{\mathrm{S}} b_{\mathrm{S}} h_{\mathrm{S}} + 2\rho_{\mathrm{P}} b_{\mathrm{P}} h_{\mathrm{P}} & 0 \\ 0 & 0 & \frac{\rho_{\mathrm{S}} b_{\mathrm{S}} h_{\mathrm{S}}^3}{12} + 2\rho_{\mathrm{P}} b_{\mathrm{P}} \left(\frac{h_{\mathrm{P}}^3}{12} + \frac{h_{\mathrm{P}} (h_{\mathrm{S}} + h_{\mathrm{P}})^2}{4} \right) \end{bmatrix}, \tag{48}$$

$$\mathbf{B}_{\mathrm{PEH}} = \begin{bmatrix} c_{\mathrm{S}} b_{\mathrm{S}} h_{\mathrm{S}} + 2c_{\mathrm{P}} b_{\mathrm{P}} h_{\mathrm{P}} & 0 & 0 \\ 0 & \frac{c_{\mathrm{S}} b_{\mathrm{S}} h_{\mathrm{S}}}{2(1+\nu_{\mathrm{S}})} + \frac{c_{\mathrm{P}} b_{\mathrm{P}} h_{\mathrm{P}}}{(1+\nu_{\mathrm{P}})} & 0 \\ 0 & 0 & \frac{c_{\mathrm{S}} b_{\mathrm{S}} h_{\mathrm{S}}^3}{12} + 2c_{\mathrm{P}} b_{\mathrm{P}} \left(\frac{h_{\mathrm{P}}^3}{12} + \frac{h_{\mathrm{P}} (h_{\mathrm{S}} + h_{\mathrm{P}})^2}{4} \right) \end{bmatrix}, \tag{49}$$

where $b_{\mathrm{S}} = b_{\mathrm{P}} = b = 1$ m in the 2D FSI implementation, and the bending stiffness of the piezoelectric beam should also be corrected to keep consistent with the plane strain assumption, as explained in



(a) Pressure distribution at $t = 2.52$ s

(b) Pressure distribution at $t = 5.73$ s

(c) Pressure distribution at $t = 8.82$ s

(d) Pressure distribution at $t = 11.91$ s

Fig. 12. Pressure distribution at different time instants, benchmark 2.

Section 4. The voltage-related equations are

$$\aleph_1(\phi,\kappa) = e_{31}b(h_S + h_P)\kappa + \frac{2b\epsilon_{33}^S\phi}{h_P} - e_{31}b(h_S + h_P)\kappa_t - \frac{2b\epsilon_{33}^S\phi_t}{h_P} - \frac{\phi}{RL_b}, \tag{50}$$

$$\aleph_2(\phi,\kappa) = -e_{31}b(h_S + h_P)\phi. \tag{51}$$

The time rate of the PEH output voltage ϕ_t is a new unknown variable to be solved. The finite element ansatz function for ϕ_t is 1 since it is independent of the space (i.e., the equipotential condition [3]). For simplicity, some terms associated with the structural non-linearity that almost do not reduce the model accuracy are omitted in Eqs. (48)–(51) [33].

5.2. A PEH immersed in a cross flow

5.2.1. Problem setup

The setup of this flow-driven PEH is adapted from a heart-valve-inspired benchmark problem [15]. The cantilevered PEH is fixed at one end on the wall of a channel and undergoes large deformation due to the cross flow, as seen in Fig. 13. The fluid velocity in x-direction at Γ_{in} is periodically changed, given by

$$v_x = 5000y(0.06 - y)\sin(20\pi t). \tag{52}$$

The bimorph length is $L_b = 2 \times 10^{-2}$ m, and the total thickness is 2×10^{-4} m, with $h_P = 8 \times 10^{-5}$ m, $h_S = 4 \times 10^{-5}$ m. Material parameters are: $\rho_F = 1260$ kgm^{-3}, $\mu_F = 1.42$ kg(ms)$^{-1}$; $\rho_S = 2800$ kgm^{-3}, $c_S = 7\times10^{10}$ Pa, $\nu_S = 0.35$; $\rho_P = 7800$ kgm^{-3}, $c_P = 6.6\times10^{10}$ Pa, $\nu_P = 0.35$, $e_{31} = -12.54$ Cm^{-2}, $\epsilon_{33}^S = 1.3281 \times 10^{-8}$ Fm^{-1}. The resistive load in the circuit is $R = 50$ kΩ. The physical scenario of this setup may be regarded as a bimorph made from aluminum alloy (the substrate) and PZT-5A (the piezo-layers) immersed in glycerine. The Reynolds number computed from $\rho_F L_b \max(v_x)/\mu_F$ is 80. The boundary conditions for the moving mesh are no-slip condition on $\Gamma_{in}\cup\Gamma_{out}\cup\Gamma_{wall}$, and slip condition on $\Gamma_{symmetry}$.

5.2.2. Numerical results

For this practical application, we set the computational time interval to be [0 s, 0.8 s], the time step size $\Delta t = 0.001$ s, the artificial material parameter of the moving mesh $\ell = 0.01$ Pa, the spectral radius $\rho_\infty^F = 0.9$, and $N_{elem} = 10368$, $N_{dof} = 131833$. The tolerance criterion for the N-R method is 5×10^{-7}.

Fig. 14 shows the displacement of the control point A and the voltage output of the PEH. In Figs. 14(a) and 14(b), the continuum solid model only takes into account the mechanical parameters of the substrate structure and the piezoelectric layers (no piezoelectric effects, no attached circuit). It can be calculated from Fig. 14(c) that the peak power output of this PEH is approximately 0.6 W ($= \frac{(\max(\phi))^2}{R}$), which seems too high for a real PEH. This high value can be explained from the perspective of the physical setting. On one hand, the deformation of the PEH is large, as seen in Fig. 14(a) or Fig. 15; on the other hand, the surfaces of the PEH are large since the width is 1 m, and they are fully covered by electrodes, so in this setting, a big number of electric charges are collected and they form alternating current in the attached circuit. Because no cancellation of the electrical outputs [51] occurs in the deformation pattern of this PEH, we deduce that 0.6 W could be a satisfactory power output of this PEH when compared with cases where the piezoelectric layers are partially covered by electrodes. One could simply modify the voltage-related Eqs. (50)–(51) to further study these cases, but this topic is highly relevant to the interior coupling of PEHs, which is however, not the focus of this paper, so we do not remark more on it.

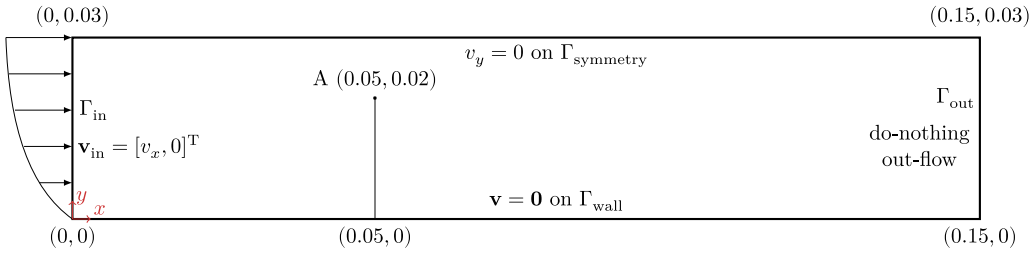
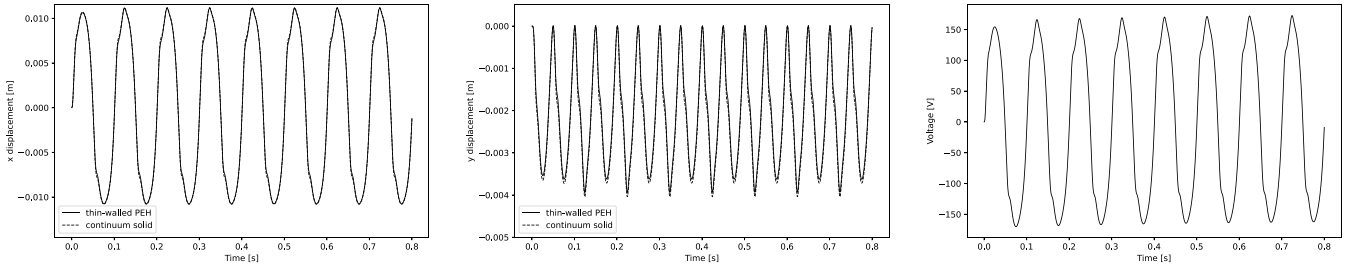


Fig. 13. Geometrical configuration and boundary conditions of the cross-flow-driven PEH, length unit [m].



(a) Displacement in x-direction (b) Displacement in y-direction (c) Voltage output

Fig. 14. Displacement of point A and voltage output of the cross-flow-driven PEH.

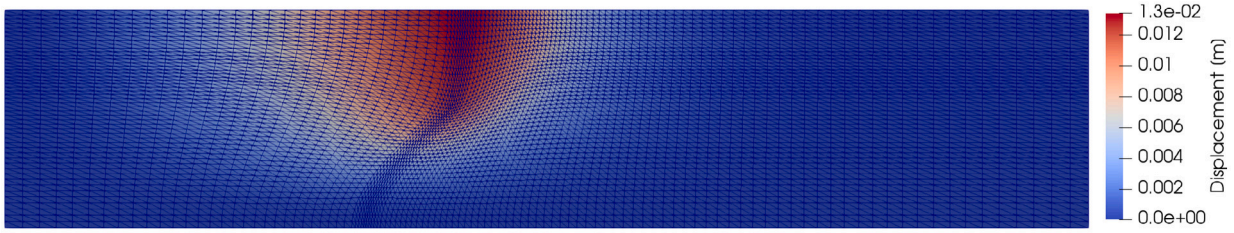


Fig. 15. Deformation of the cross-flow-driven PEH at $t = 0.425$ s.

5.3. A PEH immersed in an axial flow

5.3.1. Problem setup

Power extraction from limit cycle oscillations (LCOs) has attracted much attention in recent years [5,6,10,13]. Briefly, LCOs are a self-induced, self-sustained vibration resulting from structural or fluid nonlinearity when the flow velocity exceeds a critical value. Although being a flutter phenomenon, LCOs are favorable in energy harvesting because the structure continuously reaps energy from the surrounding fluid while its vibration magnitude does not constantly increase. The numerical example in this section is a PEH operating in LCOs.

The setup is a thin-walled PEH immersed in a uniform axial flow with the velocity at the inlet $v_\infty = 15$ ms^{-1}, as shown in Fig. 16, which is adapted from [52]. The cantilevered PEH is fixed at point C $(0.12, 0.3)$, and its free end is initially at point A $(0.7, 0.3)$. The bimorph length is $L_{\text{b}} = 5.8 \times 10^{-1}$ m, and the total thickness is 5×10^{-4} m, with $h_{\text{P}} = 1 \times 10^{-4}$ m, $h_{\text{S}} = 3 \times 10^{-4}$ m. Material parameters are: $\rho_{\text{F}} = 20$ kgm^{-3}, $\mu_{\text{F}} = 0.2$ kg(ms)$^{-1}$; $\rho_{\text{S}} = 2800$ kgm^{-3}, $c_{\text{S}} = 7 \times 10^{10}$ Pa, $\nu_{\text{S}} = 0.35$; $\rho_{\text{P}} = 7800$ kgm^{-3}, $c_{\text{P}} = 6.6 \times 10^{10}$ Pa, $\nu_{\text{P}} = 0.35$, $e_{31} = -12.54$ Cm^{-2}, $\epsilon^S_{33} = 1.3281 \times 10^{-8}$ Fm^{-1}. The resistive load in the circuit is $R = 50$ kΩ. In this scenario, the structure materials are still aluminum alloy and PZT-5A, but the fluid is an artificial material to ensure that LCOs take place at a low Reynolds number ($\rho_{\text{F}} L_{\text{b}} v_\infty / \mu_{\text{F}} = 870$). The fluid-to-structure mass ratio $\bar{m}_{\text{FS}}$ is defined by

$$\bar{m}_{\text{FS}} = \frac{\rho_{\text{F}} L_{\text{b}}}{\rho_{\text{S}} h_{\text{S}} + 2\rho_{\text{P}} h_{\text{P}}}, \tag{53}$$

which influences a lot the flutter critical velocity as well as the structural deformation patterns in LCOs [52], and $\bar{m}_{\text{FS}} = 4.83$ for the above setup. No-slip condition on $\Gamma_{\text{in}} \cup \Gamma_{\text{out}}$ and slip condition on Γ_{wall} are prescribed as the boundary conditions for the moving mesh.

5.3.2. Numerical results

In this example, the computational time interval is [0 s, 1 s], the time step size $\Delta t = 0.001$ s, the artificial material parameter of the moving mesh $\ell = 0.001$ Pa, the spectral radius $\rho^{\text{F}}_\infty = 0.8$, and $N_{\text{elem}} = 9576$, $N_{\text{dof}} = 121611$. The tolerance criterion for the N-R method is 1×10^{-8}. To start the simulation, in the first 0.01 s, an acceleration in $y-$direction $l_{perturbation} = -1000 \times (x - 0.12)$ ms^{-2} is applied to the PEH and v_∞ is set to be 0. After 0.01 s, the perturbation load is removed and $v_\infty = 15$ ms^{-1} is recovered.

Figs. 17(a)–17(b) show the electromechanical response of the PEH over the computational time, and Fig. 17(c) shows typical deformed shapes (snapshots) of the structure after it enters LCOs. If comparing Fig. 17(b) with Fig. 14(c), we find that although the PEH in this setup is much longer than the PEH in Section 5.2, the output voltage/power (peak power value approximately 0.015 W) is much lower in this setup. One non-negligible reason is that the deformation patterns in this setup, as seen in Fig. 17(c) or Fig. 18, have certain strain nodes where the dynamic strain distribution changes sign, consequently leading to strong cancellations of the electrical outputs if electrodes continuously cover the PEH surfaces [51]. Therefore, an optimized distribution of electrodes is of great significance to improve the electrical performance of the cantilevered PEH when it is operating in other than the first vibration mode. The current simulations are time-consuming and thus disadvantageous for optimization design, so a parameterized reduced order model is to be developed in the future to investigate the optimal configuration of flow-driven PEHs.

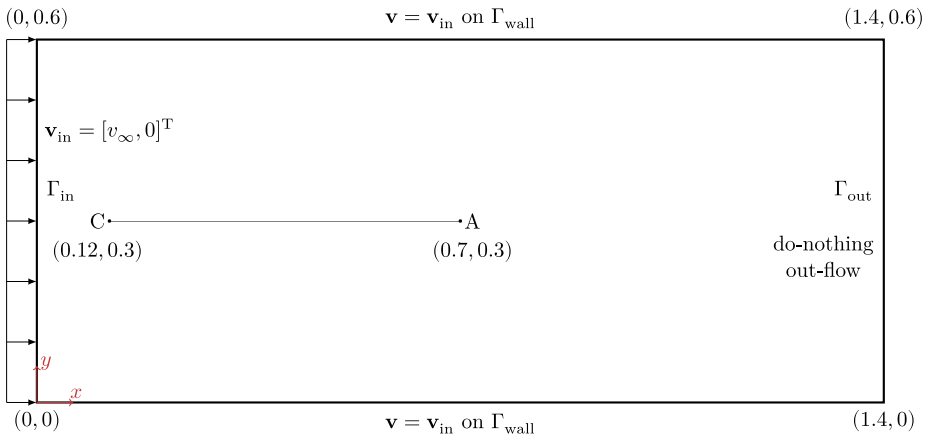
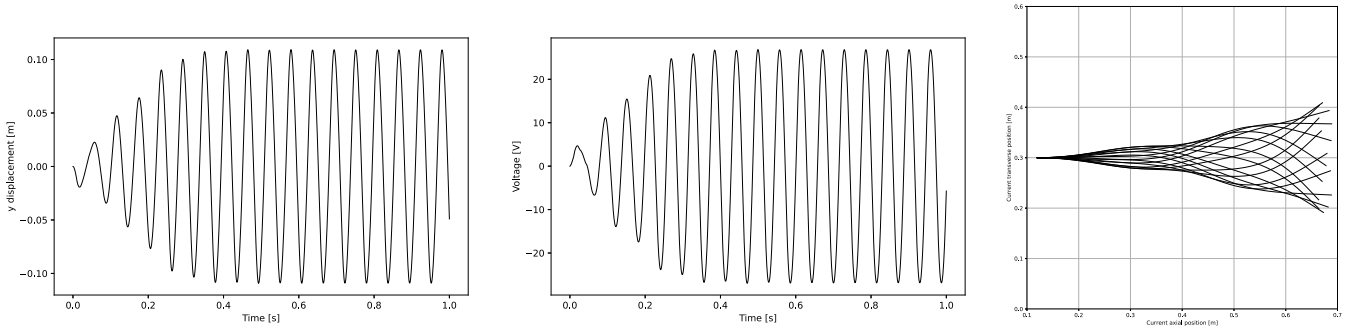
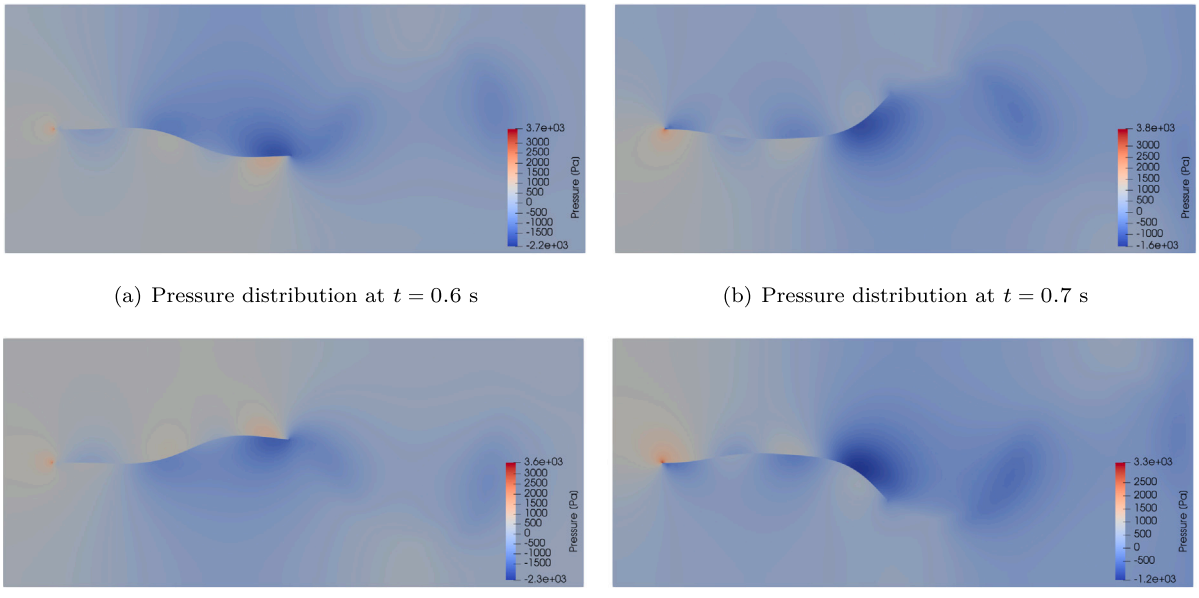


Fig. 16. Geometrical configuration and boundary conditions of the axial-flow-driven PEH, length unit [m].



(a) Displacement in y-direction (b) Voltage output (c) Deformed shapes

Fig. 17. Displacement of point A, voltage output, and deformed shapes of the PEH in limit cycle oscillations.



(a) Pressure distribution at $t = 0.6$ s (b) Pressure distribution at $t = 0.7$ s

(c) Pressure distribution at $t = 0.8$ s (d) Pressure distribution at $t = 0.9$ s

Fig. 18. Pressure distribution at different time instants of the PEH in limit cycle oscillations.

6. Conclusions

A monolithic solution scheme well tailored for thin-walled flow-driven piezoelectric energy harvesters (PEHs) based on fluid–structure interaction (FSI) is hierarchically presented: from the classical FSI setting where volumetric representation for the structure is employed, to the special FSI setting where the structure is thin enough to be represented as a non-volumetric model, and finally to the specific application where the structure is a thin-walled PEH. Besides the interior multiphysics coupling involved by the PEH itself, the challenge

arising from the specific application, when compared with the classical FSI setting, is the strong discontinuity of the pressure solution along the fluid–solid interface since the structure is geometrically simplified as a line (surface). This challenge is overcome by the splitting-fluid-domain method, which is validated against two popular FSI benchmark problems. Two numerical examples to illustrate how to apply this framework to typical flow-driven PEHs are provided at the end of this work. Study on flow-driven PEHs using the Navier–Stokes equations is limited, so the current work could be a valuable reference for the community, especially when considering that the proposed framework is fully monolithic, and appropriate to investigate the well established beam-like PEH models interacting with a flow. When the Reynolds number is high, some other computational techniques such as introducing stabilization terms or pre-conditioning methods may be needed to obtain usable solutions from the proposed framework. Given that the simulations in this work are computationally expensive, it is necessary to further establish a parameterized reduced order model to realize the optimization design of flow-driven PEHs.

CRediT authorship contribution statement

Lan Shang: Methodology, Software, Writing – original draft. **Christophe Hoareau:** Methodology, Supervision, Validation, Writing – review & editing. **Andreas Zilian:** Conceptualization, Methodology, Supervision, Writing – review & editing, Funding acquisition.

Declaration of competing interest

The authors declare that they have no known competing financial interests or personal relationships that could have appeared to influence the work reported in this paper.

Acknowledgments

The authors gratefully acknowledge the support of the Luxembourg National Research Fund under the PRIDE programme (PRIDE17/12252781) as well as the European Union's Horizon 2020 research and innovation programme under grant agreement No 811099.

References

[1] J. Wang, L. Geng, L. Ding, H. Zhu, D. Yurchenko, The state-of-the-art review on energy harvesting from flow-induced vibrations, Appl. Energy 267 (2020) 114902.
[2] Y. Amini, H. Emdad, M. Farid, An accurate model for numerical prediction of piezoelectric energy harvesting from fluid structure interaction problems, Smart Mater. Struct. 23 (9) (2014) 095034.
[3] S. Ravi, A. Zilian, Simultaneous finite element analysis of circuit-integrated piezoelectric energy harvesting from fluid-structure interaction, Mech. Syst. Signal Process. 114 (2019) 259–274.
[4] A. Erturk, W. Vieira, C. De Marqui Jr., D.J. Inman, On the energy harvesting potential of piezoaeroelastic systems, Appl. Phys. Lett. 96 (18) (2010) 184103.
[5] J. Dunnmon, S. Stanton, B. Mann, E. Dowell, Power extraction from aeroelastic limit cycle oscillations, J. Fluids Struct. 27 (8) (2011) 1182–1198.
[6] C. De Marqui Jr., D. Tan, A. Erturk, On the electrode segmentation for piezoelectric energy harvesting from nonlinear limit cycle oscillations in axial flow, J. Fluids Struct. 82 (2018) 492–504.
[7] C. De Marqui, W.G. Vieira, A. Erturk, D.J. Inman, Modeling and analysis of piezoelectric energy harvesting from aeroelastic vibrations using the doublet-lattice method, J. Vib. Acoust. 133 (1) (2011).
[8] C.R. dos Santos, D.R. Pacheco, H.E. Taha, M.Y. Zakaria, Nonlinear modeling of electro-aeroelastic dynamics of composite beams with piezoelectric coupling, Compos. Struct. 255 (2021) 112968.
[9] D. Li, Y. Wu, A. Da Ronch, J. Xiang, Energy harvesting by means of flow-induced vibrations on aerospace vehicles, Prog. Aerosp. Sci. 86 (2016) 28–62.
[10] D.T. Akcabay, Y.L. Young, Hydroelastic response and energy harvesting potential of flexible piezoelectric beams in viscous flow, Phys. Fluids 24 (5) (2012) 054106.
[11] A. Mehmood, A. Abdelkefi, M. Hajj, A. Nayfeh, I. Akhtar, A. Nuhait, Piezoelectric energy harvesting from vortex-induced vibrations of circular cylinder, J. Sound Vib. 332 (19) (2013) 4656–4667.
[12] G. Huang, Y. Xia, Y. Dai, C. Yang, Y. Wu, Fluid–structure interaction in piezoelectric energy harvesting of a membrane wing, Phys. Fluids 33 (6) (2021) 063610.
[13] S. Chawdhury, G. Morgenthal, A partitioned solver to simulate large-displacement fluid–structure interaction of thin plate systems for vibration energy harvesting, Comput. Struct. 224 (2019) 106110.
[14] J. Donea, S. Giuliani, J.-P. Halleux, An arbitrary Lagrangian-Eulerian finite element method for transient dynamic fluid-structure interactions, Comput. Methods Appl. Mech. Engrg. 33 (1–3) (1982) 689–723.
[15] D. Kamensky, M.-C. Hsu, D. Schillinger, J.A. Evans, A. Aggarwal, Y. Bazilevs, M.S. Sacks, T.J. Hughes, An immersogeometric variational framework for fluid–structure interaction: Application to bioprosthetic heart valves, Comput. Methods Appl. Mech. Engrg. 284 (2015) 1005–1053.
[16] C.S. Peskin, The immersed boundary method, Acta Numer. 11 (2002) 479–517.
[17] F.P. Baaijens, A fictitious domain/mortar element method for fluid–structure interaction, Internat. J. Numer. Methods Fluids 35 (7) (2001) 743–761.
[18] R. van Loon, P.D. Anderson, F.N. van de Vosse, S.J. Sherwin, Comparison of various fluid–structure interaction methods for deformable bodies, Comput. Struct. 85 (11–14) (2007) 833–843.
[19] J.P. Sheldon, S.T. Miller, J.S. Pitt, et al., Methodology for comparing coupling algorithms for fluid-structure interaction problems, World J. Mech. 4 (02) (2014) 54.
[20] A. Erturk, D.J. Inman, An experimentally validated bimorph cantilever model for piezoelectric energy harvesting from base excitations, Smart Mater. Struct. 18 (2) (2009) 025009.
[21] J. Dietl, A. Wickenheiser, E. Garcia, A timoshenko beam model for cantilevered piezoelectric energy harvesters, Smart Mater. Struct. 19 (5) (2010) 055018.
[22] C.D. Gatti, M. Febbo, S.P. Machado, S. Osinaga, A piezoelectric beam model with geometric, material and damping nonlinearities for energy harvesting, Smart Mater. Struct. (2020).
[23] A. Zilian, A. Legay, The enriched space–time finite element method (EST) for simultaneous solution of fluid–structure interaction, Internat. J. Numer. Methods Engrg. 75 (3) (2008) 305–334.
[24] M. Landajuela, M. Vidrascu, D. Chapelle, M.A. Fernández, Coupling schemes for the FSI forward prediction challenge: comparative study and validation, Int. J. Numer. Methods Biomed. Eng. 33 (4) (2017) e2813.
[25] C.A. Howells, Piezoelectric energy harvesting, Energy Convers. Manage. 50 (7) (2009) 1847–1850.
[26] T. Richter, T. Wick, Finite elements for fluid–structure interaction in ALE and fully Eulerian coordinates, Comput. Methods Appl. Mech. Engrg. 199 (41–44) (2010) 2633–2642.
[27] J. Hron, S. Turek, A monolithic FEM/multigrid solver for an ALE formulation of fluid-structure interaction with applications in biomechanics, in: Fluid-Structure Interaction, Springer, 2006, pp. 146–170.
[28] A. Shamanskiy, B. Simeon, Mesh moving techniques in fluid-structure interaction: robustness, accumulated distortion and computational efficiency, Comput. Mech. 67 (2) (2021) 583–600.
[29] T. Wick, Fluid-structure interactions using different mesh motion techniques, Comput. Struct. 89 (13–14) (2011) 1456–1467.
[30] B. Hübner, E. Walhorn, D. Dinkler, A monolithic approach to fluid–structure interaction using space–time finite elements, Comput. Methods Appl. Mech. Engrg. 193 (23–26) (2004) 2087–2104.
[31] E. Reissner, On one-dimensional finite-strain beam theory: the plane problem, Z. Angew. Math. Phys. ZAMP 23 (5) (1972) 795–804.
[32] H. Irschik, J. Gerstmayr, A continuum-mechanics interpretation of Reissner's nonlinear shear-deformable beam theory, Math. Comput. Model. Dyn. Syst. 17 (1) (2011) 19–29.
[33] L. Shang, C. Hoareau, A. Zilian, A geometrically nonlinear shear deformable beam model for piezoelectric energy harvesters, Acta Mech. 232 (12) (2021) 4847–4866.
[34] S. Basting, A. Quaini, S. Čanić, R. Glowinski, Extended ALE method for fluid–structure interaction problems with large structural displacements, J. Comput. Phys. 331 (2017) 312–336.
[35] K. Bäumler, E. Bänsch, A subspace projection method for the implementation of interface conditions in a single-drop flow problem, J. Comput. Phys. 252 (2013) 438–457.
[36] O. Zienkiewicz, R. Taylor, D. Fox (Eds.), Chapter 8 - treatment of constraints: Contact and tied interfaces, in: The Finite Element Method for Solid and Structural Mechanics (Seventh Edition), Seventh Edition, Butterworth-Heinemann, Oxford, 2014, pp. 235–275.
[37] A.W. Bergersen, A. Slyngstad, S. Gjertsen, A. Souche, K. Valen-Sendstad, turtleFSI: A robust and monolithic FEniCS-based fluid-structure interaction solver, J. Open Source Softw. 5 (50) (2020) 2089.
[38] J. Chung, G. Hulbert, A time integration algorithm for structural dynamics with improved numerical dissipation: the generalized-α method, J. Appl. Mech. 60 (2) (1993) 371–375.

[39] K.E. Jansen, C.H. Whiting, G.M. Hulbert, A generalized-α method for integrating the filtered Navier–Stokes equations with a stabilized finite element method, Comput. Methods Appl. Mech. Engrg. 190 (3–4) (2000) 305–319.
[40] Y. Bazilevs, V.M. Calo, T.J. Hughes, Y. Zhang, Isogeometric fluid-structure interaction: theory, algorithms, and computations, Comput. Mech. 43 (1) (2008) 3–37.
[41] C. Kadapa, W. Dettmer, D. Perić, A fictitious domain/distributed Lagrange multiplier based fluid–structure interaction scheme with hierarchical B-spline grids, Comput. Methods Appl. Mech. Engrg. 301 (2016) 1–27.
[42] M. Joosten, W. Dettmer, D. Perić, On the temporal stability and accuracy of coupled problems with reference to fluid–structure interaction, Internat. J. Numer. Methods Fluids 64 (10–12) (2010) 1363–1378.
[43] T.J. Ypma, Historical development of the Newton–Raphson method, SIAM Rev. 37 (4) (1995) 531–551.
[44] C. Taylor, P. Hood, A numerical solution of the Navier-Stokes equations using the finite element technique, Comput. & Fluids 1 (1) (1973) 73–100.
[45] J. Reddy, On locking-free shear deformable beam finite elements, Comput. Methods Appl. Mech. Engrg. 149 (1–4) (1997) 113–132.
[46] A. Logg, K.-A. Mardal, G. Wells, Automated Solution of Differential Equations By the Finite Element Method: The FEniCS Book, Vol. 84, Springer Science & Business Media, 2012.
[47] S. Balay, S. Abhyankar, M.F. Adams, S. Benson, J. Brown, P. Brune, K. Buschelman, E. Constantinescu, L. Dalcin, A. Dener, V. Eijkhout, W.D. Gropp, V. Hapla, T. Isaac, P. Jolivet, D. Karpeev, D. Kaushik, M.G. Knepley, F. Kong, S. Kruger, D.A. May, L.C. McInnes, R.T. Mills, L. Mitchell, T. Munson, J.E. Roman, K. Rupp, P. Sanan, J. Sarich, B.F. Smith, S. Zampini, H. Zhang, H. Zhang, J. Zhang, PETSC/TAO users manual, (ANL-21/39 - Revision 3.16) Argonne National Laboratory, 2021.
[48] P.R. Amestoy, I.S. Duff, J.-Y. L'excellent, Multifrontal parallel distributed symmetric and unsymmetric solvers, Comput. Methods Appl. Mech. Engrg. 184 (2–4) (2000) 501–520.
[49] L. Failer, T. Richter, A parallel Newton multigrid framework for monolithic fluid-structure interactions, J. Sci. Comput. 82 (2) (2020) 1–27.
[50] S. Turek, J. Hron, Proposal for numerical benchmarking of fluid-structure interaction between an elastic object and laminar incompressible flow, in: Fluid-Structure Interaction, Springer, 2006, pp. 371–385.
[51] A. Erturk, P.A. Tarazaga, J.R. Farmer, D.J. Inman, Effect of strain nodes and electrode configuration on piezoelectric energy harvesting from cantilevered beams, J. Vib. Acoust. 131 (1) (2009).
[52] L. Tang, M.P. Païdoussis, J. Jiang, Cantilevered flexible plates in axial flow: energy transfer and the concept of flutter-mill, J. Sound Vib. 326 (1–2) (2009) 263–276.